PhosphoThr Peptide Binding Globally Rigidifies Much of the FHA Domain from Arabidopsis Receptor Kinase-Associated Protein Phosphatase[†,‡]

Zhaofeng Ding,[§,||] Gui-in Lee,[§,||,⊥] Xiangyang Liang,[§] Fabio Gallazzi,[#] A. Arunima,[§] and Steven R. Van Doren*[,§]

Department of Biochemistry, 117 Schweitzer Hall, University of Missouri, Columbia, Missouri 65211, and Molecular Biology Program, 125 Chemistry, 601 South College Avenue, University of Missouri, Columbia, Missouri 65211

Received March 3, 2005; Revised Manuscript Received May 30, 2005

ABSTRACT: A net increase in the backbone rigidity of the kinase-interacting FHA domain (KI-FHA) from the Arabidopsis receptor kinase-associated protein phosphatase (KAPP) accompanies the binding of a phosphoThr peptide from its CLV1 receptor-like kinase partner, according to ^{15}N NMR relaxation at 11.7 and 14.1 T. All of the loops of free KI-FHA display evidence of nanosecond-scale motions. Many of these same residues have residual dipolar couplings that deviate from structural predictions. Binding of the CLV1 pT868 peptide seems to reduce nanosecond-scale fluctuations of all loops, including half of the residues of recognition loops. Residues important for affinity are found to be rigid, i.e., conserved residues and residues of the subsite for the key pT+3 peptide position. This behavior parallels SH2 and PTB domain recognition of pTyr peptides. PhosphoThr peptide binding increases KI-FHA backbone rigidity (S^2) of three recognition loops, a loop nearby, seven strands from the β-sandwich, and a distal loop. Compensating the trend of increased rigidity, binding enhances fast mobility at a few sites in four loops on the periphery of the recognition surface and in two loops on the far side of the β-sandwich. Line broadening evidence of microsecond- to millisecond-scale fluctuations occurs across the six-stranded β-sheet and nearby edges of the β-sandwich; this forms a network connected by packing of interior side chains and H-bonding. A patch of the slowly fluctuating residues coincides with the site of segment-swapped dimerization in crystals of the FHA domain of human Chfr. Phosphopeptide binding introduces microsecond- to millisecond-scale fluctuations to more residues of the long 8/9 recognition loop of KI-FHA. The rigidity of this FHA domain appears to couple as a whole to pThr peptide binding.

FHA domains[1] bind phosphothreonine- and phosphoserine-containing partners in diverse eukaryotic signaling pathways that include DNA damage repair, cell proliferation, pre-mRNA splicing, forkhead transcription factors, Ring-finger proteins, and kinesins (*1*). Several high-resolution structures of FHA domains have appeared (*2*−*8*), but no detailed studies of their dynamics. Flexibility often appears to correlate with binding events, including affinity of protein modules for peptides (*9*−*11*). Residue-specific effects on the affinity of SH2 domains for phosphotyrosine peptides are not fully explained by the structures but do correlate with rigidity of interfacial side chains (*12*). Peptide-binding dependent changes in backbone motions of the c-Src SH3 domain help explain its unfavorable entropy of peptide binding and show that the binding stabilizes the SH3 domain both near and far from the interface (*13*). Investigation of the dynamic character of an FHA domain should add insights into behaviors affecting binding and stability.

The FHA domain investigated herein is from Arabidopsis kinase-associated protein phosphatase (KAPP), a key downstream regulator of receptor-like protein kinase (RLK) signaling pathways in plants (*14*). KAPP has a C-terminal protein phosphatase 2C (PP2C) domain that dephosphorylates RLK partners to attenuate the activation of the receptor complex (*15*). KAPP was shown to interact with RLKs from Arabidopsis that include HAESA (formerly RLK5) (*14*), CLAVATA1 (*16*), RLK4 (*17*), TMK1 (*17*), WAK1 (*18*), FLS2 (*19*), BAK1 (*20*), and SERK1 (*21*). KAPP uses its kinase-interacting FHA domain (KI-FHA) to bind epitopes of RLKs activated by phosphorylation of serine or threonine residues. KI-FHA minimally comprises 119 amino acids, i.e., residues 180 to 298 of KAPP (*22*). The solution structure of KI-FHA is a sandwich of a five-stranded mixed β-sheet with six-stranded antiparallel β-sheet (*7*), like most other structures of FHA domains (*2*, *3*, *5*) and SMAD MH2 domains (*23*), despite sequence identities of less than 20% (*7*). The six-

[†] This research was supported by NSF Grant MCB0111589 to S.R.V.D. The Varian Inova 600 and Bruker DRX-500 spectrometers were funded in part by NSF Grants DBI0070359 and CHE8908304. NMRFAM is supported by the National Center for Research Resources.

[‡] The NMR relaxation data and their model-free interpretation are available for free and bound KI-FHA under BMRB accession codes 5841 and 6474 at www.bmrb.wisc.edu.

* To whom correspondence should be addressed: E-mail: vandorens@missouri.edu. Phone: 1 (573) 882-5113. Fax: 1 (573) 884-4812.

[§] Department of Biochemistry, University of Missouri.

[||] These authors contributed equally to this work.

[⊥] Current address: Department of Chemistry, 225 Prospect St., Yale University, New Haven, CT 06520.

[#] Molecular Biology Program, University of Missouri.

[1] Abbreviations: FHA domain, Forkhead-associated domain; HPLC, high-pressure liquid chromatography; KAPP, kinase-associated protein phosphatase; LC−ESI-MS, liquid chromatography−electrospray ionization mass spectrometry; NOE, nuclear Overhauser effect; RDC, residual dipolar coupling; RLK, receptor-like kinase of plants; R_1, spin−lattice or longitudinal relaxation rate; R_2, spin−spin or transverse relaxation rate; SVD, singular value decomposition.

10.1021/bi050414a CCC: $30.25 © 2005 American Chemical Society
Published on Web 07/08/2005

stranded β-sheet is an array of three β-hairpins: the 1/2, 10/11, and 7/8 β-hairpins (see below). The 5/6 β-hairpin lies in the middle of the five-stranded β-sheet. Sequence identity among diverse FHA domains is restricted to Gly211, Arg212, Ser226, His229, and Asn250 in KI-FHA numbering (*22*) of the 3/4, 4/5, and 6/7 loops on the edge of the five-stranded β-sheet that forms a surface for binding phosphorylated peptides and proteins (*3*, *4*, *7*). The 8/9 and 10/11 loops also appear to contribute to the phosphoprotein (RLK) recognition surface of KI-FHA from KAPP (*7*). A second surface on an independent face of FHA domains was proposed to be a potential self-recognition surface (*7*) and coincides with the β-hairpin that rearranges to make the segment-swapped dimer reported in the FHA domain of Chfr (*6*). Crystallographic B factors of FHA domains are low, especially in the β-strands (*5*), suggesting rigidity. Phosphopeptide binding does not appear to alter the structure of FHA domains significantly (*4*, *6*, *24*−*26*). This suggests that FHA domains may use a rigid, preformed surface for recognizing phosphoprotein partners.

Many protein−protein interaction sites do, however, have some flexibility revealed by NMR relaxation, often fluctuating over the microsecond to millisecond range (*12*, *13*, *27*−*33*). NMR relaxation rates result from the density of motions that reorient the bond probed, described by spectral density functions that are Fourier transforms of time correlation functions of the bond reorientation. The model-free formalism estimates primarily the amplitude and secondarily the time scale of intramolecular motions faster than the rotational diffusion of globular proteins (several nanoseconds), by fitting spectral density functions (*34*, *35*). The amplitude of fast internal bond reorientations can be estimated from the generalized order parameter S^2 that ranges from a value of 1.0 for full restriction to 0.0 for full lack of restriction (*34*, *36*). The model-free approach also can yield a line broadening term that results from fluctuations occurring on a time scale of microseconds to milliseconds. Alternatively, ^{15}N relaxation data are occasionally interpreted by the reduced spectral density approach. Examples of its application in molecular recognition are refs *33*, *37*. Without explicit modeling of protein tumbling, this approach suggests frequency distribution of amide bond reorientations at ^{1}H and ^{15}N Larmor precession frequencies, as well as much lower frequencies (*38*−*41*). Another means of finding structural averaging from picoseconds to tens of milliseconds is to evaluate agreement of residual dipolar couplings (RDCs), measured from weakly aligned NMR samples, with the static structural model (*42*, *43*). Comparison of the RDC fits with relaxation data can help assess structural averaging (*44*).

This first investigation of binding-linked mobility changes of an FHA domain compares the backbone dynamics of representative KI-FHA from Arabidopsis KAPP, free and bound to a pThr peptide we identified from its CLAVATA1 (CLV1) receptor-like kinase partner. CLV1 is required in Arabidopsis for balancing proliferation and differentiation of shoot and floral meristems. KAPP negatively regulates CLV1 in plant development (*45*). ^{15}N relaxation data from two magnetic fields are interpreted using both the model-free formalism (*34*−*36*) and a reduced spectral density function. Structural fitting of residual dipolar couplings provides an independent assay sensitive to additional time scales. All the loops manifest fluctuations in nanoseconds in the free state, but fewer such cases in the bound state. In the bound state, many residues have increased rigidity or S^2 whether near or far from the phosphopeptide binding site. Around seven residues have clearly decreased rigidity or S^2 as well. Fluctuations on the microsecond to millisecond scale map to a larger swath and a smaller patch of the six-stranded β-sheet.

MATERIALS AND METHODS

Preparation of KI-FHA. GST-tagged KI-FHA, containing Arabidopsis KAPP residues 180−313, was expressed in *Escherichia coli*, enriched with ^{15}N, and purified as described (*46*). After proteolytic removal of the N-terminal GST tag, a linker of Gly-Pro-Leu-Gly-Ser remained at the N-terminus of KI-FHA; the NMR-observable amides of the Leu-G1y-Ser of this linker are assigned KAPP residue numbers of 177−179. Purified KI-FHA was exchanged into 20 mM sodium phosphate (pH 6.3), 120 mM NaCl, and 7% D_2O for NMR. NMR samples of KI-FHA were 0.33 to 0.6 mM, the solubility limit.

Synthesis, Purification, and NMR Uses of CLV1 pT868 Peptide. The pT868 peptide, comprising residues 863−875 of the receptor kinase CLAVATA1 of Arabidopsis, was synthesized with an Advanced ChemTech 396 multiple peptide synthesizer (Louisville, KY) using standard Fmoc chemistry and solid-phase synthesis. Each Fmoc amino acid was coupled at least twice, except for the building blocks for the phosphothreonine and the subsequent amino acid that were coupled three times. Cleavage and side chain deprotection were achieved by treating the resin with 87.5% trifluoroacetic acid/2.5% thioanisole/2.5% phenol/2.5% water/2.5% ethanedithiol/2.5% triisopropylsilane. All reagents were HPLC or peptide synthesis grade and obtained from Fluka (Milwaukee, WI), Novabiochem (San Diego, CA), or VWR Scientific (St. Louis, MO). The crude product obtained was characterized by HPLC (Beckmann Coulter, Fullerton, CA) and LC−ESI-MS (Thermo Finnigan, San Jose, CA). The product was purified to greater than 80% by semipreparative HPLC using an in-house-optimized multistep gradient. ^{15}N−^{1}H TROSY at 22 °C monitored the effects of the CLV1 pT868 peptide on the KI-FHA amide spectrum when titrated up to a 4:1 ratio of peptide:protein. A sample of 0.795 mM pT868 peptide and 0.53 mM KI-FHA, providing ~94% saturation at the K_D of 20 μM, was used to measure a full set of standard relaxation data at each of two magnetic field strengths. A sample of 1.16 mM pT868 peptide and 0.33 mM KI-FHA, providing ~98% saturation at the K_D of 20 μM, was used to measure standard in-phase R_2 and TROSY-enhanced, relaxation-compensated R_2 at 600 MHz.

^{15}N NMR Relaxation Measurements. Spectra monitoring ^{15}N R_1 and R_2 relaxation rates and ^{15}N{^{1}H} steady-state NOE were acquired at 25 °C at both 600 and 500 MHz. Relaxation dispersion experiments were collected at 22 °C at 600 MHz. A Varian Inova 600 MHz spectrometer (University of Missouri) was used with either a high-sensitivity 5 mm ^{1}H-{^{13}C/^{15}N} cryogenic probe with shielded *z* gradient coil or a 5 mm HCN triple resonance probe fitted with an *xyz* gradient coil. The Bruker DRX-500 spectrometer at the University of Missouri was used with an 8 mm triple resonance probe with an actively shielded *z* gradient coil (Nalorac, Martinez, CA). The Bruker DMX-500 at NMRFAM was used for ^{15}N-

{^{1}H} steady-state NOE and R_1 at 500 MHz as it is fitted with a very sensitive 5 mm Cryoprobe with shielded *z* gradient coil. The temperature settings of Missouri's 500 and 600 MHz instruments were calibrated using ethylene glycol from room temperature upward and using methanol below room temperature. The actual temperatures are within 1 °C of the nominal temperatures and within 1 °C between the two instruments. The 600 MHz R_1 and R_2 pulse sequences used sensitivity-enhanced gradient-based coherence selection (*47*), implemented in Biopack. Cross-correlation was suppressed from R_1 and R_2 spectra (*48*). For good water suppression with cryogenic probes and economy of pulses for the 8 mm probe, home-implemented 3-9-19 WATERGATE (*49*) versions of sequences of ref *50* were used for ^{15}N{^{1}H} steady-state NOE, 500 MHz R_1 and R_2. The relaxation-compensated CPMG pulse sequence of ref *51* was applied to the free state of KI-FHA and the TROSY-enhanced version (*52*) to the bound state, using the Inova 600 for each. τ_{cp} delays were in both cases set for 2 ms and 7.5 ms π pulse spacing, to identify sites of exchange broadening on the millisecond scale.

Using relaxation-compensated CPMG sequences with $\tau_{cp} = 1$ ms (π pulse spacing of 2 ms), total relaxation delays were 16, 32, 48, 64, 80, 96 ms using the sequence of ref *51* or 8, 32, 64, 96, 128, and 160 ms using the sequence of ref *52*. At $\tau_{cp} = 3.75$ ms (π pulse spacing of 7.5 ms) total delays were 30, 60, 90, and 120 ms using the sequence of ref *51* or 30, 60, 90, 120, 150, and 180 ms using the sequence of ref *52*. Relaxation delay periods at 500 MHz were 20*, 60, 120*, 240, 400*, 600 and 860* ms for R_1 and 16*, 32, 48*, 64, 80*, 112, 144* ms for R_2. Asterisks (*) indicate points duplicated for estimating uncertainties in peak heights. 500 MHz R_1 data of free KI-FHA were found to reproduce well between Missouri's DRX-500 with conventional probe and NMRFAM's DMX-500 with Cryoprobe. Delay times at 600 MHz were 10, 20*, 50, 100*, 200, 350*, 500, and 700* ms for R_1 and 10*, 30, 50*, 70, 90*, 110, and 130* ms for R_2. For KI-FHA in the free state, the 600 MHz R_1 and R_2 results from the conventional probe were repeated with the cryogenic probe and averaged. NMR spectra were processed using Sybyl 6.8 or NMRPipe 2.3 (*53*). Uncertainties in R_1 and R_2 relaxation rates were generated by relaxation fitting simulations with SPARKY 3 (*54*) using 40 iterations with addition of Gaussian-distributed random noise. To obtain ^{15}N-{^{1}H} NOEs, spectra were measured with and without 3.5 s of proton saturation, in an interleaved manner to maintain identical sample conditions. The nonsaturated reference spectra had relaxation delays of 9.2 s at 500 MHz and 12 s at 600 MHz to allow water magnetization to recover completely and avoid saturation transfer. Identical pairs of NOE spectra were collected in triplicate, except for the free state at 500 MHz collected in duplicate, to evaluate standard deviations for each residue. Standard rules of statistical error propagation were applied to arithmetic combinations of relaxation rates.

Reduced Spectral Density Analysis of ^{15}N Relaxation. The spectral density function, $J(\omega)$, for an N−H bond vector describes the frequency spectrum of its reorientation. $J(\omega)$ decreases monotonically with frequency ω and has nearly zero slope at high frequency, i.e., $J(\omega_H + \omega_N) = J(\omega_H) = J(\omega_H - \omega_N)$. (Recall that ω_N is negative.) Consequently, three spectral density functions for each amide are sufficient and well-approximated from measurements of just ^{15}N R_1 and R_2 and {^{1}H}−^{15}N NOE enhancement. The three spectral density expressions resulting are (*38*−*40*)

$$J_{eff}(0) = [6/(3d^2 + 4c^2)](-R_1/2 + R_2 - 3\sigma/5) \quad (1)$$

$$J(\omega_N) = [4/(3d^2 + 4c^2)](R_1 - 7\sigma/5) \quad (2)$$

$$J(0.87\omega_H) = 4\sigma/(5d^2) \quad (3)$$

$$\sigma = (\mathrm{NOE} - 1)(\gamma_N/\gamma_H)R_1 \quad (4)$$

where $d = \mu_0 h\gamma_N\gamma_H\langle r_{NH}^{-3}\rangle/(8\pi^2)$; $c = \omega_N(\sigma_{||} - \sigma_\perp)/\sqrt{3}$; $\sigma_{||} - \sigma_\perp$ is the chemical shift anisotropy estimated to be −170 ppm; γ_H and γ_N are the gyromagnetic ratios of ^{1}H and ^{15}N; and ω_H and ω_N are the Larmor frequencies of ^{1}H and ^{15}N. $J(\omega)$ at $\omega = 0$, ω_N, and $0.87\omega_H$ were estimated from both 500 and 600 MHz relaxation data. The reduced spectral mapping approach needs no models of internal motion or of anisotropy in Brownian tumbling of the protein.

Model-Free Analysis of ^{15}N Relaxation. Model-free calculations were performed using the ModelFree 4.1 suite of programs provided by Prof. Arthur G. Palmer (*55*). Estimates of τ_m and anisotropy of the rotational diffusion tensor were obtained from R_2/R_1 ratios using the program TENSOR2 (*56*) after filter coarse- and fine-filtering out residues undergoing motion on the picosecond to nanosecond or microsecond to millisecond time scales (*57*); see Results. The ^{15}N CSA was set to the approximation of −170 ppm (*9*, *58*). To anticipate systematic effects upon S^2 of the unknown variation in ^{15}N CSA (*59*) of KI-FHA, parallel model-free calculations were fixed to a range of other CSA values. At −150 ppm, S^2 averages 0.015 ± 0.019 *above* S^2 at −170 ppm. At −190 ppm, S^2 averages 0.029 ± 0.026 *below* S^2 at −170 ppm. The uncertainties for R_1 and R_2 were set to 5% of their values as suggested (*60*). Uncertainties in the dynamics parameters were obtained using 400 step Monte Carlo simulations carried out using Modelfree 4.1. Under the assumption of a wobbling-in-a-cone motional model, the amplitude of the maximal cone semiangle of N−H bond excursions can be estimated from order parameter *S* using the relationship (*34*).

$$S = \frac{\cos(\theta) + \cos^2(\theta)}{2} \quad (5)$$

Selection of Spectral Density Expressions. Relaxation rates were fitted to one of five forms of spectral density functions (Table 1), where τ_m and $D_{||}/D_\perp$ were fixed to estimates from R_2/R_1 ratios (Table 2). To accommodate data from two magnetic fields leading to higher model-free χ^2 errors and to avoid underfitting and bias (*61*), the long-established Akaike's information criterion (AIC) (*62*) was used as the principal method of statistical model selection as described (*61*). Akaike's information criterion is computed as $\chi^2 + 2k$, where k is the number of parameters evaluated from among S_s^2, τ_e, R_{ex}, and S_f^2 (*61*, *62*). AIC was used to test need to let τ_e range up to 2 ns in expressions 2 and 4 of Table 1. By monitoring $R_1^{500\ MHz}/R_1^{600\ MHz}$ after a correction for picosecond internal motion, the PINATA algorithm suggested nanosecond-scale motions in additional residues with ratio <0.96 (*63*). The τ_e term of these residues was allowed to range up to 1 ns. The suitability of use of 1 to 2

Table 1: Spectral Density Functions Used To Fit Relaxation Data in the Extended Lipari−Szabo Model-Free Approach[a]

model	fit parameters	spectral density function
1	S^2	$J(\omega) = (2/5)\{(S^2\tau_m)/[1 + (\omega\tau_m)^2]\}$
2	S^2, τ_e	$J(\omega) = (2/5)\{(S^2\tau_m)/[1 + (\omega\tau_m)^2] + [(1 - S^2)\tau]/[1 + (\omega\tau)^2]\}$
3	S^2, R_{ex}	$J(\omega) = (2/5)\{(S^2\tau_m)/[1 + (\omega\tau_m)^2]\}$
4	S^2, τ_e, R_{ex}	$J(\omega) = (2/5)\{(S^2\tau_m)/[1 + (\omega\tau_m)^2] + [(1 - S^2)\tau]/[1 + (\omega\tau)^2]\}$
5	S_s^2, S_f^2, τ_e	$J(\omega) = (2S_f^2/5)\{(S_s^2\tau_m)/[1 + (\omega\tau_m)^2] + [(1 - S_s^2)\tau]/[1 + (\omega\tau)^2]\}$

[a] $\tau = \tau_e\tau_m/(\tau_e + \tau_m)$, where τ_m is the isotropic rotational correlation time and τ_e is the effective correlation time for internal motions. $S^2 = S_f^2S_s^2$ is the square of the generalized order parameters. S_f^2 and S_s^2 are the squares of the order parameters for the internal motions on the fast and slow time scales.

Table 2: Average Filtered Relaxation Parameters of KI-FHA, Free and Bound to pT868[a]

		coarse-filtered[b]				fine-filtered[c]					
state of KI-FHA	field, T	n^b	$^{15}N\{^1H\}$ $\overline{NOE}$	$\overline{R_1}$, s^{-1}	$\overline{R_2}$, s^{-1}	n^c	$^{15}N\{^1H\}$ $\overline{NOE}$	$\overline{R_1}$, s^{-1}	$\overline{R_2}$, s^{-1}	τ_m,[d] ns	$D_\parallel/D_\perp$[d]
free	11.74	83	0.76	2.07	11.6	46	0.76	2.05	11.5	7.57 ± 0.08	0.81 ± 0.07
	14.1	80	0.78	1.89	12.6	43	0.79	1.85	12.3		
bound to pT868[e]	11.74	57	0.75	1.91	14.4	39	0.72	1.87	14.2	10.70 ± 0.07	1.21 ± 0.06
	14.1	84	0.80	1.41	16.9[f] (16.2)[g]	42	0.80	1.35	16.4[f] (16.1)[g]		

[a] NOE, R_1, R_2, and R_2/R_1 were trimmed prior to averaging. [b] Coarse filtering employed Normadyn software to remove residues with NOE < 0.65 or with $T_2 \leq \overline{T_2} + \sigma_{T_2}$ unless $T_1 \geq \overline{T_1} + \sigma_{T_1}$ (*57*). Number of residues after filtration is *n*. [c] Fine filtering removed residues poorly fitted by simple model-free expressions 1 and 2 (Table 1). Residues with exchange broadening suggested by relaxation dispersion at 600 MHz or statistical model section were removed. Residues suggested to have nanosecond-scale motions by $J(\bar{\omega}_N = 61\ MHz) \geq \overline{J(\bar{\omega}_N)} + \sigma_{J(\bar{\omega}N)}$ were also removed. Number of residues after filtration is *n*. [d] Rotational correlation time τ_m and the $D_\parallel/D_\perp$ ratio were estimated using the fine-filtered set of residues, their 600 MHz R_1 and R_2 relaxation data, Tensor2 (56), and PDB coordinates 1MZK. [e] Except where noted, KI-FHA was present at 0.53 mM and the peptide at 1.5-fold excess, suggesting 94% peptide saturation of KI-FHA since K_D is ~20 μM. [f] These values result from increasing the peptide excess to 3.5-fold, boosting peptide saturation of the 0.33 mM KI-FHA to 98%. [g] Parenthesized values derive from R_2 measured after dilution of KI-FHA to 0.23 mM with 0.35 mM pT868 peptide. These conditions decreased peptide saturation of KI-FHA to ~88%. Uncertainties in R_2 at 0.23 mM exceed differences from R_2 at higher concentration and saturation.

ns τ_e was confirmed by elevated $J(\omega_N = 61\ MHz)$ (eq 2) since the baseline at each spectral density frequency marks the rigid structural core (*11*). To justify use of the exchange broadening term R_{ex} (expressions 3 and 4 in Table 1), *F*-testing of model-free χ^2, using data from the two fields, was required to show a *P* value <0.25 in addition to satisfying AIC. Alternatively, relaxation dispersion data with increased line broadening at slower CPMG pulsing rate, i.e., R_2(7.5 ms) − R_2(2 ms) beyond uncertainty above the baseline, was considered clear evidence of exchange on the millisecond scale and sufficient justification for use of R_{ex}.

Residual Dipolar Coupling Analysis. RDCs were measured using liquid crystals that align in the magnetic field, introducing a small net average alignment (<0.001) of KI-FHA. $^1D_{NH}$ values were measured using 0.5 mM KI-FHA in the presence of Pf1 phage (*64*) at 9.6 mg/mL and using 0.4 mM KI-FHA in 5% (w/v) C12E6/hexanol liquid crystalline medium (*65*). RDCs were obtained by comparing coupled ^{15}N IPAP-HSQC spectra of KI-FHA in the absence of orienting media against spectra of KI-FHA weakly oriented using the phage or PEG/hexanol media. $^1D_{NH}$ values of successive sets of five neighboring residues were fitted by singular value decomposition (SVD) to the four lowest energy structural models of KI-FHA (PDB code 1MZK) to obtain alignment tensor parameters as described (*44*). The application here is novel in using a group of NMR structures rather than an X-ray structure. In simulating the range of uncertainty of the alignment parameter S_{ZZ}, estimated uncertainty in atomic coordinates of 0.3 Å and of 1 Hz in measurements of $^1D_{NH}$ values were included in 512 × 1024 fits introducing random noise of this size. Repetition for the group of NMR structures in effect incorporated further structural uncertainty.

RESULTS

^{15}N Relaxation in Free and PhosphoThr Peptide-Bound States. ^{15}N NMR relaxation parameters of KI-FHA, free and bound to an excess of a 13-mer pThr peptide from CLAVATA1 (CLV1), were determined at 298 K, at both 500 and 600 MHz to enhance insight into the amplitude and time scale of backbone dynamics. The peptide, dubbed CLV1 pT868, comprises residues 863−875 of the Arabidopsis CLAVATA1 receptor-like kinase (RLK): PEYAY(pT)-LKVDEKS. Multiple sequence alignment of kinase domains of RLKs indicates that the threonine that we phosphorylated in this CLV1 pT868 peptide corresponds to Ser1060 of the BRI1 RLK, one of two neighboring residues phosphorylated at the C-terminal end of the activation loop of kinases (*66*). This suggests that pT868 of CLV1 might also be phosphorylated in vivo, making it the most likely of our KI-FHA-binding phosphopeptide candidates to be physiologically relevant. At 298K, CLV1 pT868 binds KI-FHA with apparent K_D of 21 μM by NMR at pH 6.3 and 16 μM by titration calorimetry at pH 7.5; details will be described elsewhere. Of 114 observable backbone amide peaks, 99 in the free state and 102 in the bound state were resolved well enough for quantitative analysis of their relaxation and dynamics. Single exponentials fit well the R_1 and R_2 relaxation rates. The exception is in 500 MHz R_1 spectra where four to five residues have anomalously fast relaxation (marked with gray squares in Figures 1b, 2b) that approaches or exceeds the theoretical limit of 3.14 s^{-1} when fitted with a single exponential; their biphasic relaxation is possibly an

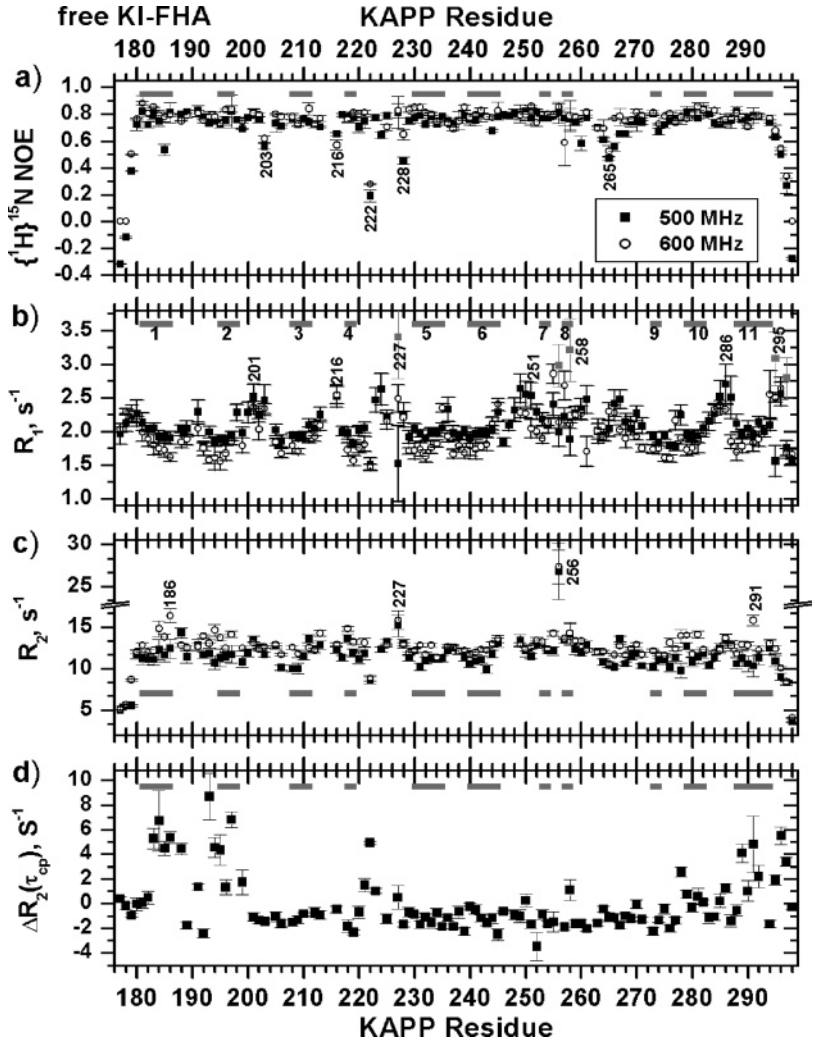

FIGURE 1: ^{15}N relaxation data of KI-FHA measured at 500 and 600 MHz and plotted vs residue from the KAPP sequence: (a) ^{15}N{^{1}H} NOE plotted as I_{sat}/I_{nonsat}, (b) spin−lattice relaxation rate constant, R_1, (c) spin−spin relaxation rate constant, R_2, and (d) relaxation-compensated CPMG measurement of $\Delta R_2 = R_2(7.5\text{ ms}) - R_2(2\text{ ms})$, where 7.5 and 2 ms are the spacing between π pulses of the CPMG trains. The temperature 25 °C was used for a−c; 22 °C was used for d. Uncertainties were estimated as described in Materials and Methods. In b, gray squares mark four cases of poor single-exponential fits due to the clear presence of a second, fast, T_2-like exponential decay; for the four affected residues, the fit of the slow decaying component is shown with black squares. The locations of β-strands are marked with gray bars in each panel. Filled squares represent 500 MHz data. Open circles represent 600 MHz data.

artifact of the exchange broadening that these particular backbone peaks undergo. In the free state of KI-FHA, the peaks of the following were too overlapped for reliable fitting: I187/L210/S223, D217/I293, N235/L283, V198/S200/E224/S248, and M246/L264. In the CLV1 pT868-bound state of KI-FHA, the spectral overlap remains in the first two peak clusters listed. With the 0.33 to 0.6 mM KI-FHA concentrations employed, particularly high S/N was assured by detection with a cryogenic probe at 600 MHz and a cryogenic probe for some of the 500 MHz data.

High backbone ^{15}N{^{1}H} NOEs indicate that KI-FHA is generally rigid on the picosecond time scale in free and CLV1 pT868-bound states (Figures 1a, 2a and Table 2). Negative NOE values and low R_2 values (Figure 1a,c) at the termini indicate their very high mobility and that the folded domain extends from KAPP residue Ser180 through Ser295. ^{15}N{^{1}H} NOEs, especially at 600 MHz, lower than 0.65 suggest such residues to be enriched in fluctuations on the picosecond to nanosecond scale. In free KI-FHA, such residues with higher amplitude fast motions are found in the 2/3 loop, 3/4 loop, 4/5 loop, and the long 8/9 loop (Figure 1a). Elevated R_1 values were shown to correlate with nanosecond internal fluctuations (*67*). In the free state, there are residues in all the loops and termini that have higher-than-average R_1 values, suggesting they may undergo nanosecond fluctuations. In the pT868-bound state of KI-FHA, all the loops show less of this trend of elevation of R_1 (Figure 2b).

Sites of high R_2 can suggest fluctuations on the microsecond to millisecond time scale. In the free state, residues with at 600 MHz R_2 exceeding 13.8 s^{-1}, i.e., >1.5σ above the coarse-filtered $\overline{R_2}$ = 12.6 s^{-1} (Table 2), came under consideration for conformational exchange broadening processes on the microsecond to millisecond scale. These residues lie in the 1/2 β-hairpin, the 3/4 loop, β4, the 4/5 loop, the 7/8 loop, β8, and 10/11 β-hairpin (Figure 1c). (The term *β-hairpin* refers to both antiparallel strands and the intervening loop). Relaxation-compensated CPMG R_2 measurements comparing averaged R_2 between faster and slower pulsing of CPMG π pulses can exaggerate the line broadening of millisecond-scale chemical exchange processes (*51*).

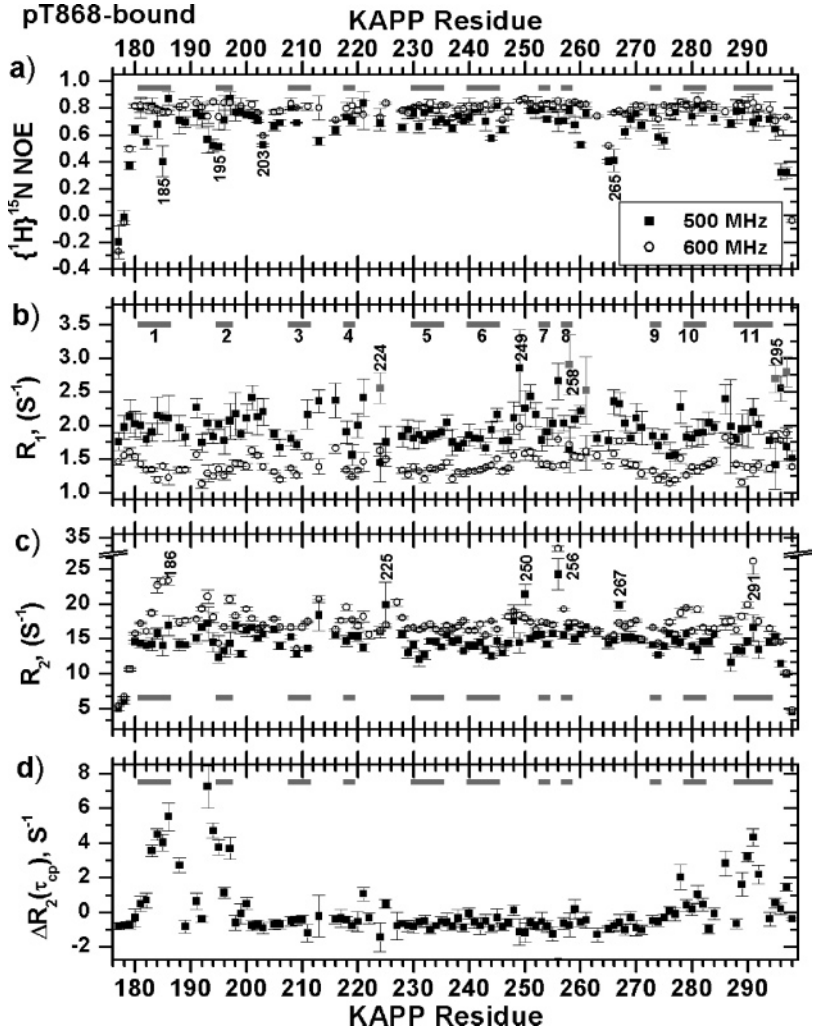

FIGURE 2: ^{15}N relaxation data of KI-FHA, bound to the CLV1 pT868 peptide at 25 °C, and plotted vs residue number from the KAPP sequence: (a) ^{15}N{^{1}H} NOE, (b) R_1, (c) R_2, and (d) $\Delta R_2 = R_2(7.5\text{ ms}) - R_2(2\text{ ms})$. The temperature 25 °C was used for a−c; 22 °C was used for d. The peptide was present at 1.5-fold excess, except for the 3.5-fold excess used for R_2 measurements in c and d at 600 MHz. The symbol code of Figure 1 is used.

Elevated $\Delta R_2 = R_2(7.5\text{ ms}) - R_2(2\text{ ms})$ in Figure 1d clearly suggest millisecond exchange broadening to occur in the 1/2 β-hairpin, the 4/5 loop, β8, the 9/10 loop, 10/11 β-hairpin, and C-terminus. Most of these residues evidently with millisecond-scale motions are found in a swath across the six-stranded β-sheet, i.e., its β1, β2, β10, and β11 strands. Similar inspection of elevated 600 MHz R_2 values with CLV1 pT868-bound present at 3.5-fold excess suggest the same segments of bound KI-FHA to undergo exchange broadening, plus the 6/7 recognition loop (Figure 2c). For the bound state, elevated $\Delta R_2 = R_2(7.5\text{ ms}) - R_2(2\text{ ms})$ in Figure 2d is very similar to that of the free state (Figure 1d), including the patterns of millisecond exchange broadening in the 1/2 β-hairpin, 10/11 β-hairpin, and C-terminus.

J(ω_N) Reduced Spectral Density Evidence of Nanosecond Motions in KI-FHA. Reduced spectral density fitting of the relaxation data (*39*, *40*) gives temporal insight into the backbone mobility of free and bound KI-FHA. Elevated $J(\omega_N)$ values, where $\omega_N = 60.8$ MHz, in free KI-FHA (Figure 3a) suggest that all of its loops and its termini have sites enriched in nanosecond-scale fluctuations. $J(\omega_N)$ values of pT868-bound KI-FHA are lower overall with fewer elevated excursions (Figure 3a). Much of the general trend to lower $J(\omega_N)$ values in the bound state may be a consequence of its slower tumbling and higher basal $J_{eff}(0)$ (not shown). In the pThr peptide-bound state, however, locally more attenuated $J(\omega_N)$ values suggest that all of the loops have residues with nanosecond fluctuations apparently quenched (Figure 3a). The following β-strands have residues with apparently fewer nanosecond fluctuations: especially β1, but also one to two residues in each of β-strands 6 through 11 (Figure 3a).

Fluctuations in the Loops of Free KI-FHA Are Corroborated by Deviations of $^{15}N-^1H$ Residual Dipolar Couplings. Residual dipolar couplings (RDCs) can respond to motional averaging over a wide, continuous range of time scales from picoseconds to tens of milliseconds (*42*, *43*), an advantage over spin relaxation studies. Deviations of measured RDCs from RDCs predicted from the alignment of the protein structure can result from static or dynamic discrepancy from the protein structural coordinates (*42*, *43*). All $^1D_{NH}$ RDCs were fitted to the whole of each of the 10 lowest energy structures from the KI-FHA ensemble (PDB code 1mzk) using PALES (*68*). Deviations of individual $^1D_{NH}$ RDCs from those predicted by fits using singular value decomposition (SVD) are represented in Figure 3b as a χ^2-like quantity that is normalized by the D_a description of the range of observed RDCs. Several loops have $^1D_{NH}$ RDCs that deviate from RDCs predicted by the structure, where L

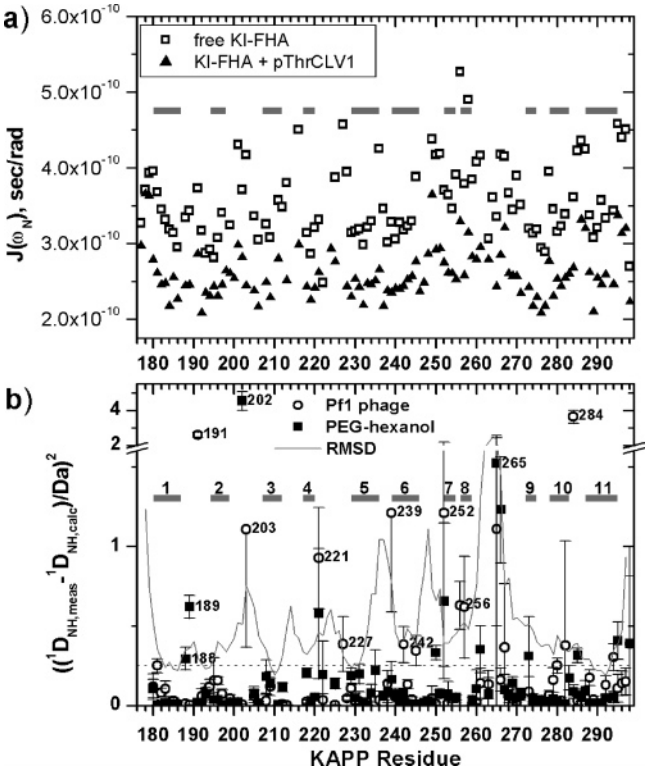

FIGURE 3: Evidence for nanosecond backbone motions. (a) Reduced spectral density function $J(\omega_N)$ plotted vs residue, where $\omega_N = 3.8 \times 10^8$ rad/s since the relaxation data were collected at 600 MHz. Open squares represent the free state, and filled triangles represent the state bound to pT868 from CLV1. (b) Sites in free KI-FHA where residual dipolar couplings (RDCs) deviate from those predicted by SVD fits to the NMR structural coordinates of KI-FHA (PDB code 1mzk). Squared deviations of individual $^1D_{NH}$ measured RDCs from those predicted by SVD fits of all RDCs to the entire backbone are normalized by D_a, the axial component of the powder pattern distribution of RDCs observed. This quantity is averaged for the 10 lowest energy NMR structures of KI-FHA.

is for loop: L1/2, L2/3, L4/5, L5/6, L6/7, L7/8, L8/9, and L10/11 loops. β8 and the C-terminus also have residues with deviating $^1D_{NH}$ RDCs (Figure 3b). A majority of the sites of $^1D_{NH}$ deviation have higher-than-average RMSD in the ensemble of structures. Most cases of $(^1D_{NH,meas} - {}^1D_{NH,calc})/D_a$ deviations in the free state (Figure 3b) have elevated $J(\omega_N)$ evidence of nanosecond-scale motions (Figure 3a,b). The $(^1D_{NH,meas} - {}^1D_{NH,calc})/D_a$ parameter appears to respond independently to many but not all possible sites of apparent nanosecond-scale motion.

We also used the method of ref *44* to fit successive quintets of $^1D_{NH}$ RDCs to the atomic coordinates of their respective fragments of the KI-FHA structural model. Deviations of molecular segments' alignment tensors from the overall protein alignment may result from dynamic or static deviations (*43*). The following segments of the backbone deviated beyond uncertainty from prediction from the coordinates using weak protein alignment in two different media: Glu185−Gln195 that span the 1/2 hairpin loop, Ala197 to Lys209 in the 2/3 loop to β3, Ala230−Trp234 in β5, Thr237−Trp241 in the 5/6 loop to β6, and Asp263 to Trp269 in the 8/9 loop (see Figure S1 and description in Supporting Information). All of these deviant segments, except for β-strand 5, are enriched in motions on the scales of either microseconds−milliseconds or nanoseconds (Figures 1d, 3a, 4).

Hydrodynamics of KI-FHA, Free and Bound to CLV1 pT868 Peptide. Rotational correlation time τ_m (overall tumbling) and rotational diffusion anisotropy can be estimated from R_2/R_1 ratios (and atomic coordinates) using rigid residues where the R_2/R_1 ratio depends only on τ_m, in the limit of small amplitude fast internal motions ($\tau_e \ll \tau_m$) (*69*). An attractive two-stage procedure for identifying such residues without discarding R_2/R_1 ratios made high or low by anisotropy of diffusion is that of ref *57*. The results of the coarse filtering stage using those authors' NormaDyn software with the 500 and 600 MHz data collected for free and bound states are presented in Table 2. Typically about 80 candidate residues, having acceptably high $^{15}N\{^1H\}$ NOE and acceptably moderate R_2, remained after coarse filtering. The purpose of the subsequent fine filtering stage is to remove additional residues poorly fit by simple model-free expressions 1 and 2 (Table 1) due to motions on the nanosecond or microsecond to millisecond scales (*57*). We enhanced the fine filtering stage by removing (1) residues with millisecond-scale exchange broadening according to relaxation dispersion (Figures 1d, 2d), (2) residues likely to have nanosecond motion due to $J(\bar{\omega}_N) \geq \overline{J(\bar{\omega}_N)} + 1\sigma$ where $\omega_N = 60.8$ MHz (Figure 3a), or (3) residues requiring the exchange broadening term R_{ex} in preliminary model-free simulations according to statistical model selection. Around 40 residues survived this enhanced fine filtering (Table 2).

The trustworthy, fine-filtered data from 600 MHz with cryogenic probe were fitted to the NMR structure of free KI-FHA (PDB accession code 1MZK) to assess correlation time and anisotropy of rotational diffusion using the TENSOR2 program of ref *56*. The ratio of the principal moments of inertia of free KI-FHA is 1.00:0.91:0.55. The free state is estimated to have τ_m of 7.57 ± 0.08 ns with $D_\parallel/D_\perp = 0.81 \pm 0.07$ (oblate) and the pT868-bound state to have τ_m of 10.70 ± 0.07 with $D_\parallel/D_\perp = 1.21 \pm 0.06$ (prolate). (Note that a prolate to oblate shift was reported for peptide binding to an SH3 domain (*13*).) For the free and bound states, both oblate and prolate axially symmetric fits are acceptable with high statistical confidence and have χ^2 similar to within 10%. Such two-minimum behavior suggests the possibility of fully anisotropic diffusion (*70*). Indeed, a fully anisotropic diffusion model is statistically significantly better for the bound state. The limitation to axial symmetry of Modelfree 4.1 used here and widely could add a very modest systematic bias, but little difference in S^2 values results from switching between oblate and prolate models for KI-FHA (not shown).

These τ_m estimates for KI-FHA at 25 °C are comparable to the τ_m values of monomers of similar size and temperature (*33*, *71*, *72*). The unlabeled free state of KI-FHA is 124 residues and 13.3 kDa by ESI-MS while the complex is 12% larger at 137 residues and 14.9 kDa. Saturation with the 1.6 kDa, 13-mer pT868 peptide increases R_2/R_1 more than expected (Table 2). The resulting increase in apparent Stokes radius with the pT868 peptide bound is around 9%. Why does the increase in τ_m upon saturation with the 1.6 kDa pT868 peptide appear to be ~1.5 ns more than expected? To investigate whether peptide binding promotes self-association, a complex of 0.53 mM KI-FHA with 1.5-fold excess of pT868 peptide was diluted 2.3-fold, resulting in perhaps a 4% average drop in R_2 values (Table 2). This decrease parallels the decrease in pT868 peptide saturation from

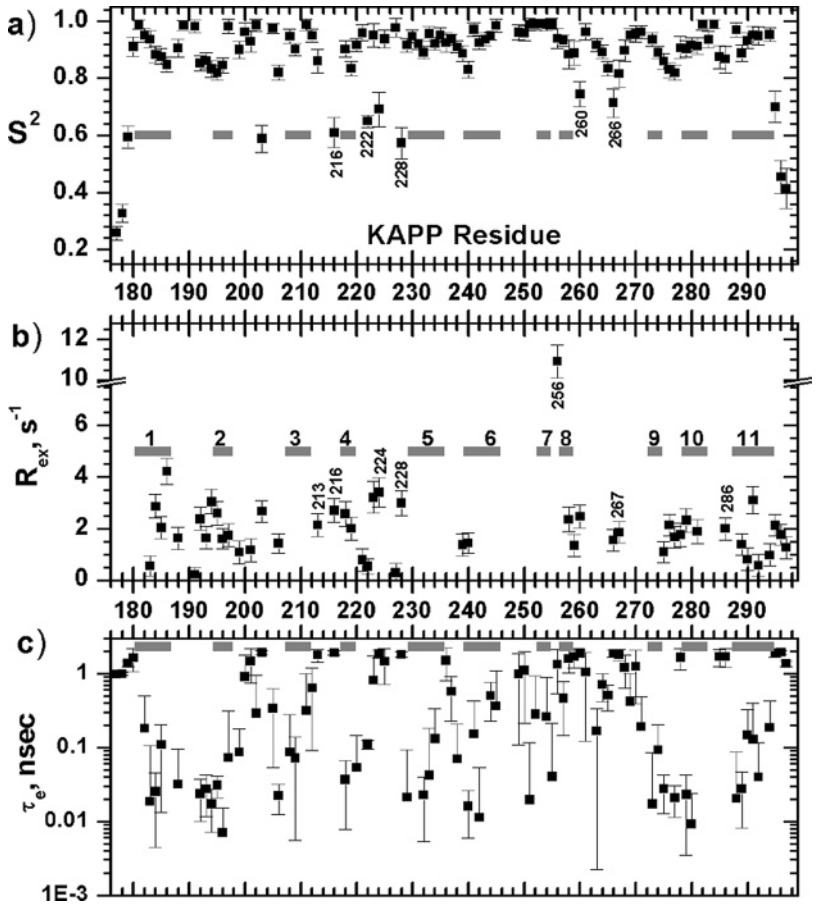

FIGURE 4: Model-free dynamics results for the free state of KI-FHA from fits of ^{15}N relaxation at two fields, 500 and 600 MHz. (a) The generalized order parameter S^2, (b) the line broadening term R_{ex}, and (c) the internal correlation time τ_e are plotted vs sequence position in KI-FHA. Locations of β-strands are marked with bars.

94% at 0.53 mM KI-FHA to 88% at 0.23 mM KI-FHA, i.e., the enhanced weighting of the free state contribution to apparent τ_m when diluted. If self-association were substantial, a larger drop in R_2 and estimated τ_m ought to have accompanied 2.3-fold dilution. A more likely alternative explanation could be that the greater extent of nanosecond fluctuations of the loops in the free state may decrease its effective Stokes radius relative to the bound state. (Note that a case of greater slowing of rotational diffusion upon peptide binding to a monomer has been reported, where coupling between altered internal motion and diffusional shape seems larger (*73*).)

Spectral Density Function Selection for Model-Free Simulations. Model-free simulations of the relaxation data proceeded with hydrodynamics parameters τ_m and $D_{\parallel}/D_{\perp}$ fixed at the values listed in Table 2. Use of relaxation data from two magnetic fields in the model-free approach more reliably defines the S^2, R_{ex} (excess line broadening), and τ_e (internal correlation time) parameters. Data at two magnetic fields also provides enough measurements to use three-parameter fits where needed. *Five* measurements were used for both the free and bound states of KI-FHA, namely, 600 MHz R_1, R_2, and NOE and 500 MHz R_1 and NOE. Omission of 500 MHz R_1 gave very similar results. The spectral density functions (Table 1) most appropriate for use in model-free simulations were chosen primarily using AIC-based statistics (*61*) augmented by other experimental identification of millisecond motion from relaxation dispersion parameter $\Delta R_2(\tau_{cp})$ (*51*) (Figures 1d, 2d) and of nanosecond motion from the reduced spectral density function $J(\omega_N = 60.8$ MHz) (*41*) (Figure 3a), as described in Materials and Methods. The spectral functions selected from among the choices of Table 1 are listed in Table S1 of Supporting Information, by residue number for free and bound states of KI-FHA.

General Model-Free Outcomes for Free and Bound States. Excluding the termini, S^2 values appear to average 0.902 and 0.946 for the free and pT868-bound states of KI-FHA, respectively. For the nonterminal residues compared in both states, $\Delta S^2_{bound-free}$ averages 0.042 with a median $\Delta S^2_{bound-free}$ of 0.036 and average uncertainty of 0.037. These suggest that phosphoThr binding results in enhanced overall rigidity on the picosecond to nanosecond scale. Model-free τ_e values (Figure 4c) are joined by elevation of both $J(\omega_N)$ (*41*) (Figure 3a) and R_1 (*67*) (Figure 1b) in suggesting nanosecond motions in all of the loops and termini of free KI-FHA except for the 1/2 loop. Fewer of these residues in the CLV1 pT868-bound state of KI-FHA show such evidence of nanosecond motions (Figures 2b, 3a, 5c, 7), suggesting that peptide binding quenches nanosecond motions globally. Where the loops are enriched with nanosecond-scale fluctuations, especially in the free state, the S^2 values can be regarded as overestimates, as established by methods that account for coupling of internal nanosecond motion with rotational diffusion (*74*, *75*). The relaxation data and model-free results for KI-FHA, free and bound to CLV1 pT868, were deposited under BMRB accession codes 5841 and 6474, respectively, at www.bmrb.wisc.edu.

pThr Peptide Binding Surface and Its Slower Dynamics. Titration of ^{15}N-enriched KI-FHA with the CLV pT868

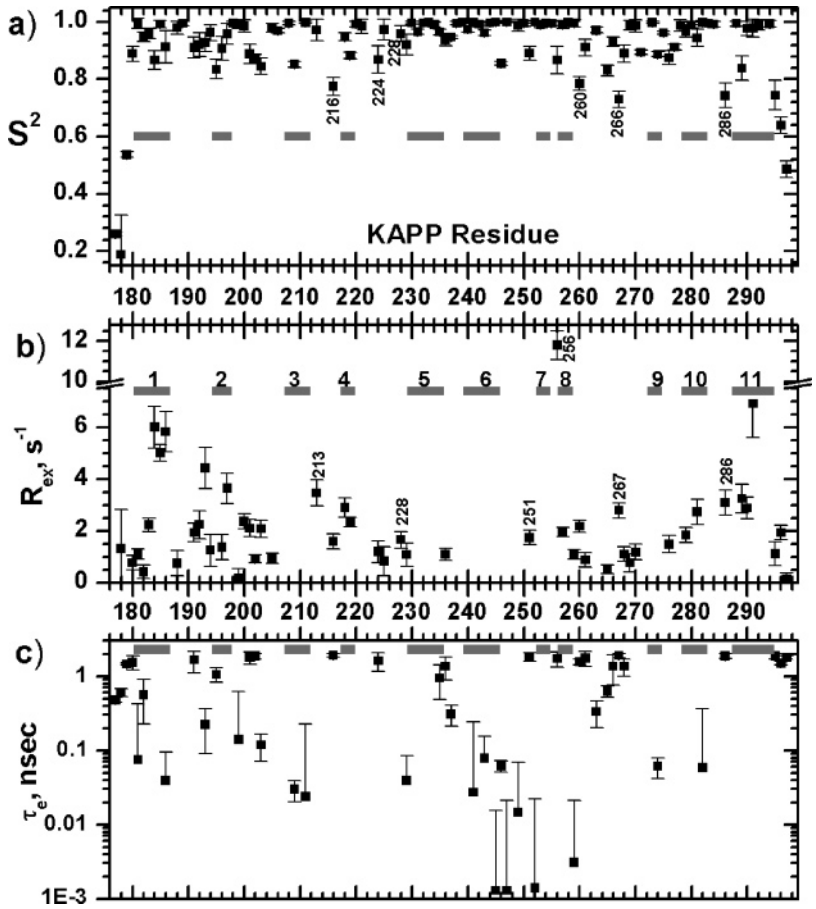

FIGURE 5: Model-free dynamics results for KI-FHA bound to CLV1 pT868 using ^{15}N relaxation collected at both 500 and 600 MHz. (a) The generalized order parameter S^2, (b) the line broadening term R_{ex}, and (c) the internal correlation time τ_e are plotted vs sequence position in KI-FHA. Locations of β-strands are marked with bars.

peptide shifted the amide peak positions of loops on one edge of the β-sandwich of KI-FHA. Significant amide chemical shift changes occur at Leu210−Val213 of the 3/4 loop; Lys221−Ser223, Val225, and Gly227−His229 of the 4/5 loop; Met246−Asn250 and Thr252 of the 6/7 loop; Asp263, Gly265, Arg267, and Trp269 of the 8/9 loop; and Gly284−Thr287 of the 10/11 loop (Figure 6c,d). Nanosecond-scale motions characterize the *free* state of several residues quite perturbed by the pT868 peptide: Arg212, Val213, Ser223, Val225, Lys228, Leu249, Asn250, Arg267, Thr285, and Thr286 (Figures 3a, 4c). Much slower conformational fluctuations over microseconds to milliseconds are shared by the free and bound states of these pT868-perturbed residues: Val213, Ser216, Lys228, Arg267, and Thr286 (Figures 4b, 5b). Exchange broadening >1 s^{-1} suggests that fluctuations in the microsecond to millisecond regime also occur at Ser223 and Glu224 in the free state (Figure 4b) and at His229 and Gly251 in the bound state (Figure 5b).

Binding Effects on Flexibility on Fast Time Scale in Recognition Interface. Largely conserved recognition loop residues shown to be essential for binding phosphorylated receptor kinase domain (*22*) are clearly rigid. Their apparent S^2 values in free/bound states are 0.99/0.999 for Gly211, 0.92/0.92 for His229, and 0.96/0.99 for Asn250 (Figures 4a, 5a). Binding appears to quench nanosecond fluctuations of Asn250 (Figures 3a, 4c, and 5c). Near the five most conserved residues in the recognition loops are nonconserved residues with greater mobility and significant changes of S^2 upon binding of the pT868 peptide from CLV1. Fluctuations in the free state of greater-than-average amplitude are suggested by apparent $S^2 \leq 0.8$ of residues of the 3/4, 4/5, and 8/9 recognition loops: Ser216, Asp222, Glu224, Lys228, Ser260, and Ser266 (Figure 4a). Lys228 and Glu224 of the 4/5 loop, Ser266 of the 8/9 loop, as well as Ser216 and Val213 of the 3/4 loop undergo striking increases in rigidity on the picosecond−nanosecond scale upon pT868 peptide binding (Figure 6). Leu220, Asp263, and Leu283 of these recognition loops are rigidified to a smaller degree. Also at the interface, Gly251 of the 6/7 loop, Arg267 of the 8/9 loop, and T286 of the 10/11 loop in contrast become more flexible on the fast time scale in the complex (Figure 6a,b).

Long-Range Effects of Binding on Fast Time Scale Motion. For a number of residues outside this binding surface for phosphorylated RLKs (Figure 6d), mobility of KI-FHA on the picosecond to nanosecond scale changes upon binding the pT868 peptide from the CLV1 RLK. In the loops of the 1/2 and 10/11 β-hairpins pointing toward the interface, residues where binding increases the amplitude of picosecond−nanosecond motions (drop in S^2) are Ala191 and Thr286 (Figure 6a,b). In the loop of the 7/8 β-hairpin distant from the interface, binding may have increased the fast motion of Ser256 (Figure 6a). By contrast, pT868 peptide binding appears to have increased rigidity in β-strands of all four of the β-hairpins. This is especially evident in both strands of the 1/2 β-hairpin, both strands of the 5/6 β-hairpin, β8 of the 7/8 β-hairpin, and more subtly in both strands of 10/11 β-hairpin (Figure 6a,b). The apparent changes in S^2 in the highly disordered termini are unlikely to be significant since

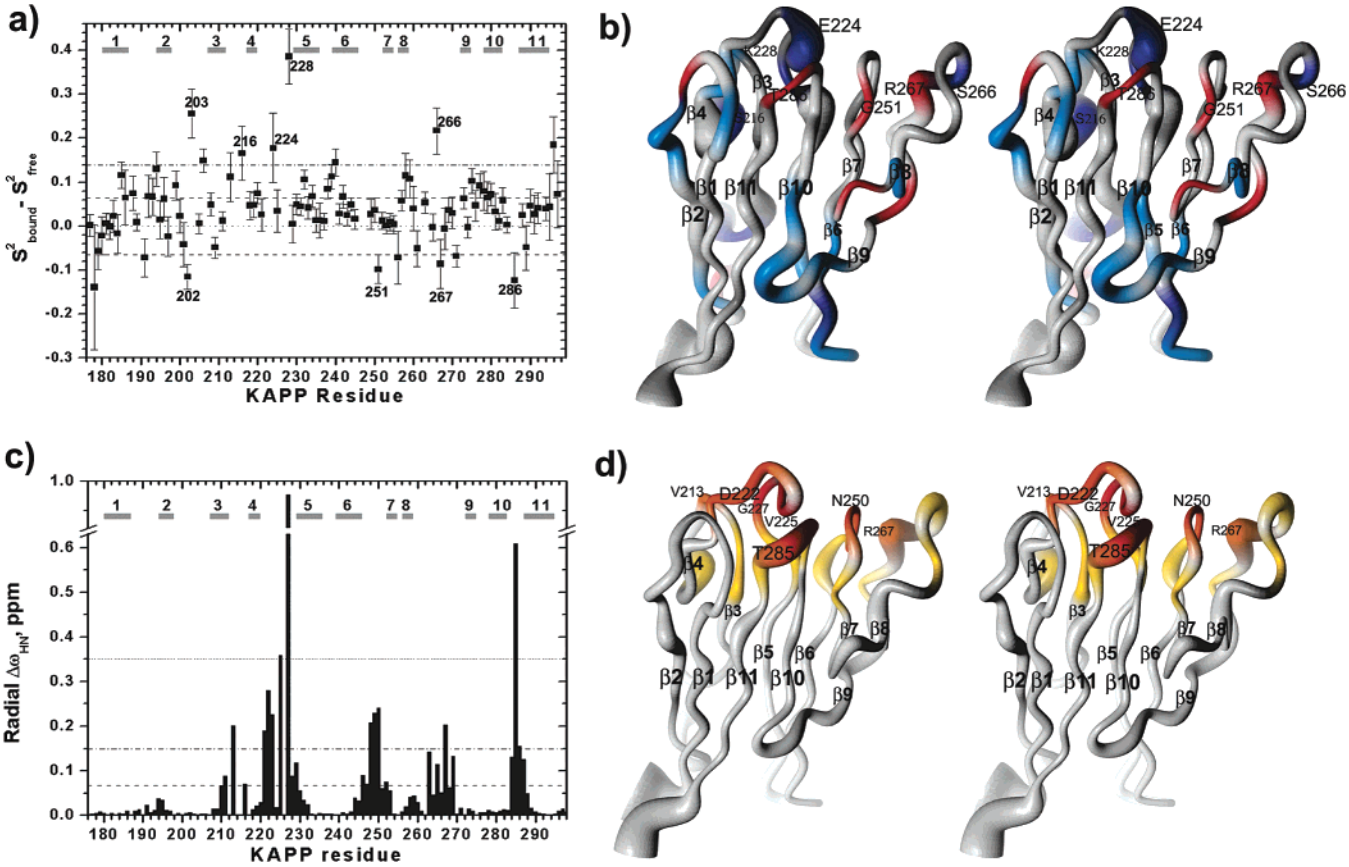

FIGURE 6: Comparison of pT868 peptide-induced changes in KI-FHA flexibility over picoseconds to nanoseconds and in amide NMR peak positions at the interface. (a) Changes in the generalized order parameter S^2 upon the binding of the pT868 peptide are plotted vs residue of KAPP. The locations of β-strands are marked with gray bars. Residues with $S^2_{bound} - S^2_{free} \geq 0.065$, marked by a dashed line, represent the upper 30-percentile of ΔS^2 values. (b) Sites of ΔS^2 are colored on the stereoview of the backbone of free KI-FHA with tube width proportional to $1 - S^2_{free}$, i.e., for the free state. In b, residues rigidified by pT868 peptide binding are colored dark blue where $S^2_{bound} - S^2_{free} > 0.14$ and lighter blue where $0.14 > \Delta S^2 > 0.065$. Residues mobilized by pT868 peptide binding are colored red where $S^2_{bound} - S^2_{free} \leq -0.065$. (c) Shifts of amide NMR peaks of KI-FHA upon addition of a 4-fold excess of the CLV1 pT868 peptide are plotted vs location in KAPP. The radial shift of the peak $\Delta\omega_{NH} = (\Delta\omega_H^2 + (\Delta\omega_N/6)^2)^{1/2}$, where $\Delta\omega_H$ and $\Delta\omega_N$ are the changes in ^{1}H and ^{15}N dimensions in ppm. (d) pT868-induced chemical shift changes, $\Delta\omega_{NH}$, are mapped onto the stereoview of the backbone of the free KI-FHA structure with tube width proportional to $1 - S^2_{bound}$, representing the bound state. Residues are colored in red where $\Delta\omega_{NH} > 0.35$, orange where $0.35 > \Delta\omega_{NH} > 0.15$, and gold where $0.15 > \Delta\omega_{NH} > 0.067$. A few of the most shifted residues are labeled. In b and d, unobservable residues are colored a darker shade of gray.

the termini lack the globular diffusion behavior needed for accurate description by the model-free approach (Figure 6a). The 2/3 loop and 9/10 loop each cross between the two β-sheet layers of the sandwich and are most distant from the binding surface. The peptide binding effect on the 2/3 loop includes mobilization of Ser202 and increased rigidity of Ser203 and Leu206 (Figure 6a). The phosphoThr peptide binding rigidifies Leu275−Asp278 of the remote 9/10 loop.

Binding Effects on Flexibility on Slow Time Scale. Exchange broadening suggests motions on the microsecond to millisecond time scale for around 49 residues in the free state and 51 residues in the bound state of KI-FHA, by relaxation dispersion (Figures 1d, 2d) or statistical need for R_{ex} term in model calculations (Figure 7). The slow fluctuations affect a contiguous swath of residues across β2, β1, β11, and β10 of the six-stranded sheet (appearing left to right in Figures 7, 8). Adjacent to this central swath are other clusters of slowly exchanging residues. At the edge of the five-stranded sheet, β4 and the 3/4 and 4/5 recognition loops are affected (Figure 7a). At the extreme opposite edge of the six-stranded sheet, residues of β8, the 7/8 loop, and the 8/9 loop manifest motions on the microsecond to millisecond scale (Figure 7a). Also exchanging are residues in the 1/2 and 10/11 loops near the binding site, the faraway 2/3 and 9/10 loops, and C-terminus. With the CLV1 pT868 peptide present at 3.5-fold excess, the peptide is expected to saturate 98% of KI-FHA based on the K_D of 20 μM. At 98% saturation, Gly265 and Lys268−Gly270 of the 8/9 peripheral recognition loop and Gly251 of the 6/7 recognition loop have exchange broadening (Figures 4b, 5b, and 7). Asp222, Gly227, and Thr285, with peaks most shifted and broadened during titration with the pT868 peptide (Figure 6a), are too broad in the peptide-saturated state for relaxation fitting.

Dissociation of CLV1 pT868 Peptide from KI-FHA. Intermediate exchange broadening during titration with the pT868 peptide can be exploited to estimate the exchange rate k_{ex}. The off-rate k_{off} is equivalent to k_{ex}, since k_{on} is not at all limiting, being of the order of $\sim 5 \times 10^7$ M^{-1} s^{-1}. The range of k_{ex} and k_{off} possible is defined by the binding-induced chemical shift changes of Gly227 of $\Delta\nu_H = 569$ Hz and Thr285 of $\Delta\nu_H = 356$ Hz at 600 MHz; spectral and thermodynamic details will be published elsewhere. Gly227 in the slow−intermediate exchange regime limits k_{ex} to the range of $2.2\Delta\nu_{H,G227} > k_{ex} > 0.01\Delta\nu_{H,G227}$, i.e., 1250 s^{-1} > k_{ex} > 5.7 s^{-1}. Thr285 in the fast−intermediate exchange regime limits k_{ex} to this range: $100\Delta\nu_{H,T285} > k_{ex} > \Delta\nu_{H,T285}$,

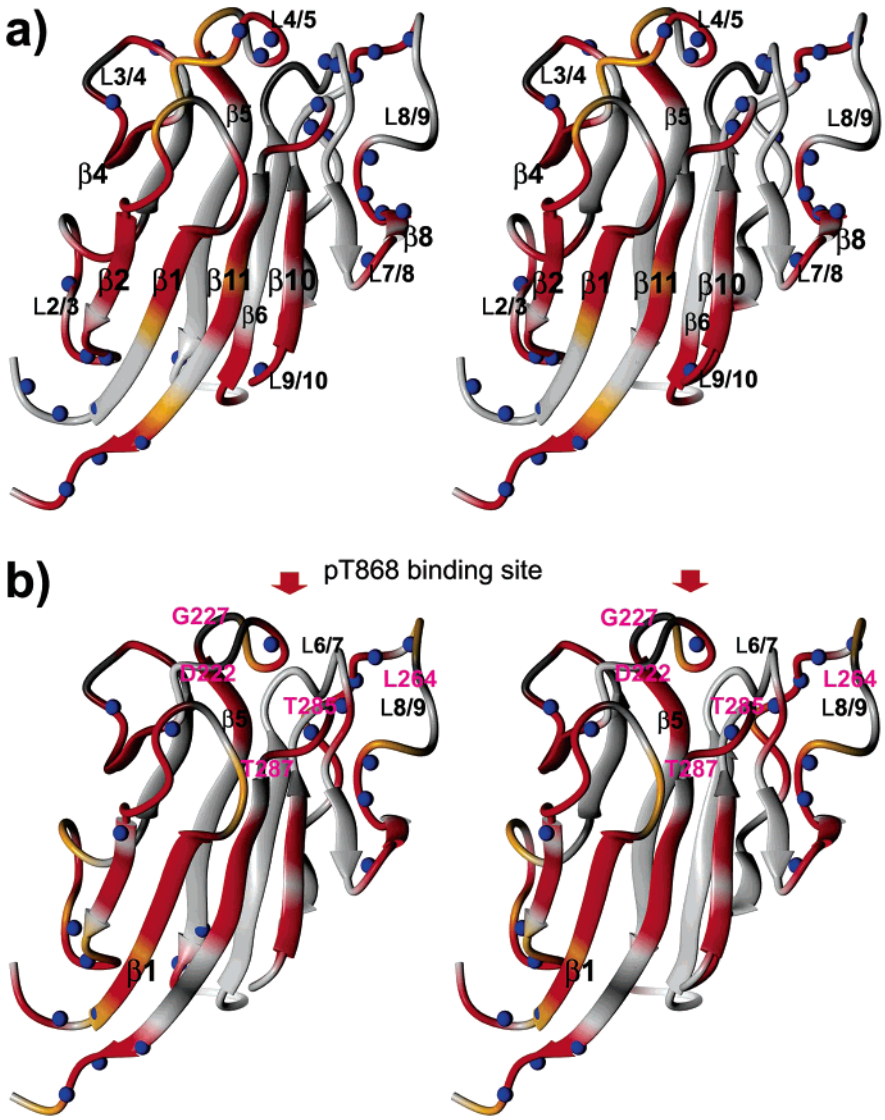

FIGURE 7: Mapping of sites of microsecond- to millisecond-scale fluctuations and of nanosecond-scale motions, of backbone amide peaks upon the KI-FHA NMR structure for the free state (a) and pT868-bound state (b). In a and b, residues with $R_{ex} > 1\ s^{-1}$ exchange broadening evidence of the slower motions are colored red and those with $1\ s^{-1} > R_{ex} > 0\ s^{-1}$ are colored orange. Residues with apparent $\tau_e > 0.7$ ns are marked with blue spheres. Unobservable residues are colored a darker shade of gray. Structural elements with R_{ex} in free KI-FHA are labeled in a. In b, residues are labeled where binding of the pT868 peptide introduces R_{ex}. The binding surface for phosphoThr peptides or phosphoproteins (receptor-like kinases such as CLV1 in plants) is indicated with red arrows. Residues in the bound state undergoing too much chemical exchange broadening for relaxation fitting are labeled in pink; these residues exhibit intermediate exchange broadening during titration with the pT868 peptide.

i.e., $35{,}600\ s^{-1} > k_{ex} > 356\ s^{-1}$. Combining these two ranges leads to the conservative estimate that k_{off} and k_{ex} lie between $356\ s^{-1}$ and $1250\ s^{-1}$ for the pT868 interaction with KI-FHA. When pT868 is present at 1.5-fold excess conferring 94% saturation of KI-FHA, additional exchange broadening is seen in recognition loops in a comparison of 600 MHz R_2 values at 94% and 98% saturation. This is most evident in the 6/7 loop, followed by the 8/9 loop, the 4/5 loop, and conserved Gly211 (Figure S2 of Supporting Information). A set of model-free results were obtained from relaxation measurements at the 1.5-fold excess of pT868 that results in ~94% saturation of KI-FHA. At 94% saturation relative to 98% saturation, more residues in recognition loops manifest chemical exchange broadening, namely, at 6/7 loop residues Met246, Leu249, Asn250, and Thr252, as well as conserved Gly211 and Asp263 and Ser266 of the 8/9 loop (Figures S2, S3 of Supporting Information). Since each of

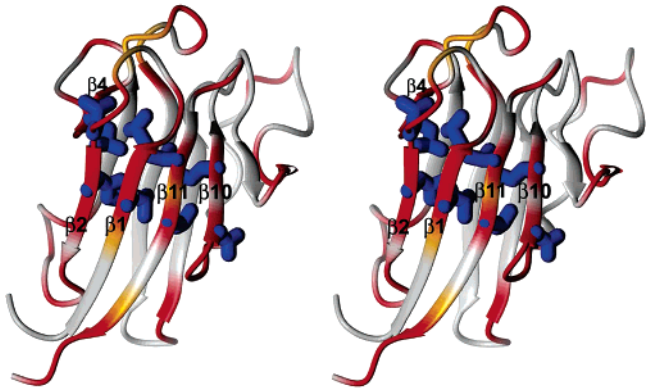

FIGURE 8: A network of two tiers of packed interior side chains, plotted in blue, where the backbone is affected by conformational exchange detected as line broadening. The color code of the backbone is that of Figure 7a.

these residues undergoes chemical shift changes upon titration with the pT868 peptide (Figure 6a), it appears likely that their broadening at 94% saturation results from the peptide's apparent off-rate of between 350 and 1250 s^{-1}.

DISCUSSION

Rigidity of Residues Conserved in the Recognition Site of FHA Domains. Along the edge of the five-stranded β-sheet, conserved Gly211, Arg212 (3/4 loop), Ser226, His229 (4/5 loop), and Asn250 (6/7 loop) (KAPP numbering) are very rigid (Figures 4a, 5a) and critical for forming the phosphoprotein binding site of FHA domains; the arginine, serine, and asparagine contact the phosphoThr of the ligand (*3*, *5*−*7*, *22*, *25*, *26*). The high rigidity of Gly211 and Arg212 of the 3/4 loop and His229 of the 4/5 loop (Figures 4, 5) is consistent with the structure-stabilizing role proposed for conserved Gly211 and His229 (KAPP numbering) (*3*). The unique conformation of absolutely conserved Gly211 could be important for positioning Arg212 to interact with the phosphate of the partner. Gly211 and Arg212 being recessed and largely buried under the interaction surface may confer their rigidity. When the S^2 values of Gly211, Arg212, His229, and Asn250 are interpreted with a diffusion-in-a-cone model of motion (*36*), the estimated amplitudes of N−H bond reorientations in picoseconds to nanoseconds have cone semiangles of 5°/2°, 11°/NA, 14°/13°, and 10°/4°, for the free/bound states, respectively. The backbone rigidity of Gly211, Arg212, His229, and Asn250 in the free state decreases energetic costs of loss of configurational entropy upon binding.

Nonconserved Residues of the Phosphoprotein-Binding Surface. Comparison of FHA domain structures of divergent sequence (*3*, *76*) suggested that KI-FHA residues Glu224 in the 4/5 loop, Leu249 in the 6/7 loop, and Thr285 in the 10/11 loop may contribute to the key pT+3 site and KI-FHA's distinctive phosphopeptide specificity (*7*). In yeast Rad53 FHA domains, two more residues appear to contact the pT+3 peptide position (*77*); the first is equivalent to Gly284 and the second possibly to Thr286 of the 10/11 loop of KAPP. The amide peaks most shifted upon addition of the CLV1 pT868 peptide (with radial $\Delta\omega_{HN} > 0.15$ ppm; Figure 6c) suggest a broad phosphoThr peptide recognition surface (Figure 6d). This same broad phosphoprotein (RLK)-binding surface is suggested by evolutionary trace analysis and extensive conservation among plant KAPPs on its flanks (*7*). Most residues of this surface are not, however, widely conserved among FHA domains (*7*). These nonconserved residues of the recognition loops can be placed in three groups of picosecond−nanosecond mobility (S^2). The first group is very rigid in both free and pT868-bound states: Lys221, Gly227, Leu249, Trp269, and Gly284. The second group is more flexible in the free state, undergoes restriction in the bound state, and is listed here with estimates of wobbling-in-cone semiangles (see eq 5) for free/bound states in parentheses: Val213 (18°/8°), Ser216 (35°/23°), Glu224 (28°/17°), Lys228 (34°/10°), and Ser266 (27°/13°). These are from solvent-exposed portions of the 3/4, 4/5, and 8/9 loops, with the central 4/5 loop seeming to be in especially intimate contact with the phosphopeptide (Figure 6). The third group at the edge of the recognition surface has increased mobility in the pT868-bound state and is listed with estimated cone semiangles: Gly251 (5°/16°) of the 6/7 loop, Arg267 (21°/26°) of the 8/9 loop, and Thr286 (18°/25°) of the 10/11 loop.

Rigidity and Role in Affinity of Residues at the pT+3 Site and Conserved Neighbors. Rigid portions of the phosphoprotein-binding surface could confer affinity to this FHA domain and others. This hypothesis derives from observations on modules binding pTyr peptides: First, the residues of a PTB domain that contact a relevant pTyr peptide are rigid, presumably promoting enthalpically favorable van der Waals contacts (*78*). Second, in the association of SH2 domains with pTyr peptides, high rigidity is characteristic of sites conferring affinity (*12*). Clearly, mostly conserved Gly211, Arg212, Ser226, His229, and Asn250 (KAPP numbering) are rigid in the free state (Figure 4) and apparently essential for affinity for receptor-like kinase domains (*22*). This behavior is consistent with the studies of pTyr peptide recognition. The pT+3 position of peptide ligands is the most important determinant of their affinity for FHA domains (*3*, *79*). The nonconserved residues that divergent FHA domains place around the pT+3 site appear to be important for affinity (*77*). These residues of KI-FHA of KAPP, namely, Gly227, Leu249, Gly284, and Thr285, are rigid (Figures 4, 5), consistent with the theme of high rigidity of residues conferring affinity (*12*, *78*).

Significance of pThr Peptide Binding-Dependent Flexibility Changes Remote from RLK Binding Site. Energetic costs of pThr peptide binding include the loss of conformational entropy of the peptide, at sites in the 3/4, 4/5, and 8/9 recognition loops, at sites in seven β-strands, and in three other loops (1/2, 2/3, and 9/10 loops) (Figure 6a,b). In the free state, there appears to be more nanosecond-scale motion than in the bound state in all five recognition loops, other loops, and β8 (Figures 3a, 4c, 5c). Since S^2 is more likely to be underestimated at these locations (*74*, *75*) in the *free* state, the binding-linked increases in rigidity and the entropic costs at these recognition loop residues could be underestimated. The modest increases in rigidity of seven of the 11 β-strands may not represent just costs in configurational entropy. The binding-dependent increases in S^2 appear to occur across networks of hydrogen-bonded residues across both β-sheets; one such network includes $\beta3-\beta5-\beta6-\beta9$ while another network includes $\beta2-\beta1-\beta11-\beta10$ (Figure 6b). The increased rigidity seen in both β-sheets suggests the possibility of improved hydrogen bonding and side chain packing or van der Waals contacts, for a favorable change in the enthalpy of the bound state. This could provide part of the compensating favorable enthalpy driving the association of pThr peptides to KI-FHA (Ding et al., to be published) and to another FHA domain (*3*). Peptide binding was also observed to rigidify and stabilize an SH3 domain both near and far from the interface (*13*). Precedent for enthalpic stabilization at long range was suggested by antibody binding to lysozyme increasing its hydrogen exchange protection to the distal side (*80*). Sites of binding-enhanced fast motions of KI-FHA seen in the 1/2, 2/3, 6/7, 7/8, 8/9, and 10/11 loops provide favorable increases in conformation entropy to compensate the entropic costs listed above.

Flexibility of Recognition Surface in View of Breadth of Specificity. Several nonconserved residues of the recognition loops are more flexible than average: Ser216 (3/4 loop); Asp222, Glu224, Lys228 (4/5 loop); Ser260, Gly265−Arg267 (8/9 loop); and Thr286 (10/11 loop). The mobility

of these in the free state appears to be on the nanosecond scale (Figures 3a, 4c). The studies of SH2 domain affinity for pTyr peptides suggest that flexibility correlates well with contact sites of little importance to affinity. Mobility on the picosecond to nanosecond scale in a recognition surface may decrease the contribution of the mobile groups to affinity by diminishing favorable, strongly distance-dependent van der Waals interactions (*12*). Flexibility in the phosphoprotein-binding surface of KI-FHA and other FHA domains might confer their breadth of specificity. An example of such flexibility could be the 8/9 loop of KI-FHA of KAPP that distinguishes it from the phosphoprotein-binding surface of other FHA domains. This 8/9 loop of KI-FHA is clearly longer, more solvent-exposed, and mobile on the nanosecond scale. The prominence and mobility of the 8/9 loop may be important in KAPP's recognition of several RLK targets in plants. Arabidopsis KAPP interacts in a phosphorylation-dependent manner with the following receptor-like kinases critically important to plant development and defense against infection: CLV1 (*81*), HAESA (*82*), WAK1 (*18*), BAK1 (*20*), SERK1 (*21*), and FLS2 (*19*). KAPP being promiscuous enough to attenuate multiple RLK-dependent signaling pathways in plants is supported moreover by KAPP being a single gene product without any known paralog of overlapping function (*17*). Yet, KAPP failed to interact with a number of kinases tested (*17*). The picosecond−nanosecond mobility of the RLK-binding surface of KI-FHA could foster the limited diversity of RLK partners recognized by KAPP. Perhaps an analogy could be drawn with the cytokine IL-2 where the flexible portion of its ligand-binding surface binds a far greater diversity than does the rigid portion (*83*). Both the picosecond−nanosecond flexibility and binding-inducible microsecond to millisecond mobility of the recognition loops could enable KI-FHA of KAPP to adjust to a minority of the 417 RLKs encoded by the Arabidopsis genome (*84*).

Significance of Microsecond to Millisecond Fluctuations of 6-Stranded β-Sheet Remote from Phosphoprotein Binding Surface. Slow fluctuations of β2, β4, and β8 on the edges of the β-sandwich of KI-FHA may simply result from their solvent exposure. The largest line broadening evidence of fluctuations on the microsecond to millisecond scale occurs at Ser256 of the 7/8 loop (Figures 4b, 5b, 7). Neighboring residues of the 7/8 β-hairpin, β10, and the 9/10 loop also display line broadening evidence of conformational exchange on the microsecond to millisecond scale (Figures 4b, 5b, and 7). This patch of slowly fluctuating residues coincides with a potential interaction surface predicted by evolutionary trace analysis to include many of the same residues of the β7/8 hairpin, β10, and the 9/10 loop (*7*). It is unlikely that a phosphoprotein partner can wrap 80° around from the phosphorecognition surface to this face of FHA domains. The β7/8−L9/10−β10 patch coincides with the site of segment-swapped dimerization in crystals of the FHA domain of human Chfr (*6*). (In concentrated solutions of the Chfr FHA domain, the dimer is a minor form relative to the predominant monomer (*6*).) Perhaps the slow conformational fluctuations of the β7/8−L9/10−β10 patch facilitate rearrangements such as the straightening of the 7/8 β-hairpin of the segment-swapped Chfr FHA dimer. The question has been raised as to whether this independent patch could be a site of dimerization of FHA domains more generally (*7*). An alternative postulate regarding the patch is that it might play a role in self-recognition of another part of the same protein chain or signaling assembly (*7*). Slow fluctuations over microseconds to milliseconds have been observed at a number of protein−protein interaction sites (*27*−*29*, *33*, *85*).

A swath of contiguous residues across the six-stranded sheet undergo exchange broadening of their amide lines (sheet in foreground of Figure 7). Most of these have interior side chains arrayed in two packed rows across β2, β1, β11, and β10, plus β4 of the other sheet (Figure 8). Among these nine side chains, four—Leu184, Ile281, Val289, and Val291—are among a dozen hydrophobic positions characteristic of the folding core of all FHA and SMAD MH2 domains (*7*). The upper row comprises Leu218 of β4, Leu194 of β2, Val186 of β1, Val289 of β11, and Ile281 of β10, progressing left-to-right across Figure 8. The lower row comprises His196 of β2, Leu184 of β1, Val291 of β11, and Asp279 of β10. The tight packing of this cluster of interior side chains plus the interstrand hydrogen bonds might coordinate the backbone motions on the microsecond to millisecond scale.

To recap, the conformational fluctuations of the loops on the nanosecond scale in the free state of KI-FHA are diminished when the pT868 peptide fragment of the CLAVATA1 receptor kinase partner is bound (Figure 3a). A network of residues across the six-stranded β-sheet undergoes conformational fluctuations on the microsecond to millisecond scale independent of binding state (Figure 8). Microsecond- to millisecond-scale fluctuations are found in a patch of residues at β7/8−L9/10−β10 corresponding to the site of crystallization-promoted, segment-swapped dimer formation in the FHA domain of human Chfr (Figure 7). With the phosphoThr peptide bound, more sites in the 6/7 and 8/9 recognition loops display evidence of microsecond- to millisecond-scale motion (Figures 5, 7). Most of the broadening in the 6/7 loop seems to result from the peptide's off-rate of several hundred per second. Peptide binding-enhanced rigidity of 10 or more residues of recognition loops and adjoining 1/2 loop is compensated by flexibility increases on the fast time scale of six residues on the periphery of the active site (Figure 6). The net overall increase in rigidity of KI-FHA phosphoThr peptide bound, with average $\Delta S^2 = 0.04$, includes increased rigidity at sites in seven β-strands (Figure 6); this suggests the possibility of long-range enhancement of favorable enthalpy to compensate entropic costs of binding. Favorable binding enthalpy is likely from the backbone rigidity at the conserved residues clearly important to affinity and from neighboring residues most likely to contact the key pT+3 position that influences affinity.

ACKNOWLEDGMENT

We thank NMRFAM (Madison, WI) for access to the cryoprobe-equipped Bruker DMX-500. We thank Professors Palmer, Marion, Zuiderweg, Bax, and Nicholson for software used in this study.

SUPPORTING INFORMATION AVAILABLE

Figure S1 showing sites of dynamic or static deviations of $^1D_{NH}$ RDCs from the NMR structure of KI-FHA, Figure S2 showing the greater extent of exchange broadening when KI-FHA is 94% saturated with pT868 peptide present at 1.5-fold excess, Figure S3 mapping onto the structure the extent

of exchange broadening when KI-FHA is 94% saturated with pT868 peptide present at 1.5-fold excess, and Table S1 listing spectral density functions selected for model-free simulations of KI-FHA from Arabidopsis KAPP. This material is available free of charge via the Internet at http://pubs.acs.org.

REFERENCES

1. Durocher, D., and Jackson, S. P. (2002) The FHA domain, *FEBS Lett. 513*, 58−66.
2. Liao, H., Byeon, I. J., and Tsai, M. D. (1999) Structure and function of a new phosphopeptide-binding domain containing the FHA2 of Rad53, *J. Mol. Biol. 294*, 1041−1049.
3. Durocher, D., Taylor, I. A., Sarbassova, D., Haire, L. F., Westcott, S. L., Jackson, S. P., Smerdon, S. J., and Yaffe, M. B. (2000) The molecular basis of FHA domain:phosphopeptide binding specificity and implications for phospho-dependent signaling mechanisms, *Mol. Cell 6*, 1169−1182.
4. Liao, H., Yuan, C., Su, M. I., Yongkiettrakul, S., Qin, D., Li, H., Byeon, I. J., Pei, D., and Tsai, M. D. (2000) Structure of the FHA1 domain of yeast Rad53 and identification of binding sites for both FHA1 and its target protein Rad9, *J. Mol. Biol. 304*, 941−951.
5. Li, J., Williams, B. L., Haire, L. F., Goldberg, M., Wilker, E., Durocher, D., Yaffe, M. B., Jackson, S. P., and Smerdon, S. J. (2002) Structural and functional versatility of the FHA domain in DNA-damage signaling by the tumor suppressor kinase Chk2, *Mol. Cell 9*, 1045−1054.
6. Stavridi, E. S., Huyen, Y., Loreto, I. R., Scolnick, D. M., Halazonetis, T. D., Pavletich, N. P., and Jeffrey, P. D. (2002) Crystal Structure of the FHA Domain of the Chfr Mitotic Checkpoint Protein and Its Complex with Tungstate, *Structure 10*, 891−899.
7. Lee, G. I., Ding, Z., Walker, J. C., and Van Doren, S. R. (2003) NMR structure of the forkhead-associated domain from the Arabidopsis receptor kinase-associated protein phosphatase, *Proc. Natl. Acad. Sci. U.S.A. 100*, 11261−11266.
8. Li, H., Byeon, I. J., Ju, Y., and Tsai, M. D. (2004) Structure of human Ki67 FHA domain and its binding to a phosphoprotein fragment from hNIFK reveal unique recognition sites and new views to the structural basis of FHA domain functions, *J. Mol. Biol. 335*, 371−81.
9. Ishima, R., and Torchia, D. A. (2000) Protein dynamics from NMR, *Nat. Struct. Biol. 7*, 740−743.
10. Stone, M. J. (2001) NMR relaxation studies of the role of conformational entropy in protein stability and ligand binding [Review], *Acc. Chem. Res. 34*, 379−388.
11. Atkinson, R. A., and Kieffer, B. (2004) The role of protein motions in molecular recognition: insights from heteronuclear NMR relaxation measurements, *Prog. Nucl. Magn. Reson. Spectrosc. 44*, 141−187.
12. Kay, L. E., Muhandiram, D. R., Wolf, G., Shoelson, S. E., and Forman-Kay, J. D. (1998) Correlation between binding and dynamics at SH2 domain interfaces, *Nat. Struct. Biol. 5*, 156−163.
13. Wang, C., Pawley, N. H., and Nicholson, L. K. (2001) The role of backbone motions in ligand binding to the c-Src SH3 domain, *J. Mol. Biol. 313*, 873−887.
14. Stone, J. M., Colinge, M. A., Smith, R. D., Horn, M. A., and Walker, J. C. (1994) Interaction of a protein phosphatase with an *Arabidopsis* Serine-Threonine Receptor Kinase, *Science 266*, 793−795.
15. Stone, J. M., Trotochaud, A. E., Walker, J. C., and Clark, S. E. (1998) Control of meristem development by CLAVATA1 receptor kinase and KAPP protein phosphatase interactions, *Plant Physiol. 117*, 1217−1225.
16. Williams, R. W., Wilson, J. M., and Meyerowitz, E. M. (1997) A possible role for kinase-associated protein phosphatase in the *Arabidopsis* CLAVATA1 signaling pathway, *Proc. Natl. Acad. Sci. U.S.A. 94*, 10467−10472.
17. Braun, D. M., Stone, J. M., and Walker, J. C. (1997) Interaction of the maize and Arabidopsis kinase interaction doamins with a subset of receptor-like protein kinases: implication for transmembrane signaling in plants, *Plant J. 12*, 83−95.
18. Park, A. R., Cho, S. K., Yun, U. J., Jin, M. Y., Lee, S. H., Sachetto-Martins, G., and Park, O. K. (2001) Interaction of the Arabidopsis receptor protein kinase Wak1 with a glycine-rich protein, AtGRP-3, *J. Biol. Chem. 276*, 26688−26693.
19. Gómez-Gómez, L., Bauer, Z., and Boller, T. (2001) Both the extracellular leucine-rich repeat domain and the kinase activity of FLS2 are required for flagellin binding and signaling in Arabidopsis, *Plant Cell 13*, 1155−1163.
20. Li, J., Wen, J. Q., Lease, K. A., Doke, J. T., Tax, F. E., and Walker, J. C. (2002) BAK1, an Arabidopsis LRR receptor-like protein kinase, interacts with BRI1 and modulates brassinosteroid signaling, *Cell 110*, 213−222.
21. Shah, K., Russinova, E., Gadella, T. W., Jr., Willemse, J., and De Vries, S. C. (2002) The Arabidopsis kinase-associated protein phosphatase controls internalization of the somatic embryogenesis receptor kinase 1, *Genes Dev. 16*, 1707−1720.
22. Li, J., Smith, G. P., and Walker, J. C. (1999) Kinase interation domain of kinase-associated protein phosphatase, a phosphoptotein-binding domain, *Proc. Natl. Acad. Sci. U.S.A. 96*, 7821−7826.
23. Huse, M., Muir, T. W., Xu, L., Chen, Y. G., Kuriyan, J., and Massague, J. (2001) The TGF beta receptor activation process: an inhibitor- to substrate-binding switch, *Mol. Cell 8*, 671−682.
24. Yuan, C., Yongkiettrakul, S., Byeon, I. J., Zhou, S., and Tsai, M. D. (2001) Solution structures of two FHA1-phosphothreonine peptide complexes provide insight into the structural basis of the ligand specificity of FHA1 from yeast Rad53, *J. Mol. Biol. 314*, 563−575.
25. Wang, P., Byeon, I.-J. L., Liao, H., Beebe, K. D., Yongkiettrakul, S., Pei, D., and Tsai, M.-D. (2000) Structure and Specificity of the Interaction between the FHA2 Domain of RAD53 and Phosphotyrosyl Peptides, *J. Mol. Biol. 302*, 927−940.
26. Byeon, I. J., Yongkiettrakul, S., and Tsai, M. D. (2001) Solution structure of the yeast Rad53 FHA2 complexed with a phosphothreonine peptide pTXXL: comparison with the structures of FHA2-pYXL and FHA1-pTXXD complexes, *J. Mol. Biol. 314*, 577−588.
27. Wyss, D. F., Dayie, K. T., and Wagner, G. (1997) The counter-receptor binding site of human CD2 exhibits an extended surface patch with multiple conformations fluctuating with millisecond to microsecond motions, *Protein Sci. 6*, 534−542.
28. Feher, V. A., and Cavanagh, J. (1999) Millisecond-timescale motions contribute to the function of the bacterial response regulator protein SpoOF, *Nature 400*, 289−293.
29. Huang, K., Ghose, R., Flanagan, J. M., and Prestegard, J. H. (1999) Backbone dynamics of the N-terminal domain in E. coli DnaJ determined by 15N- and 13CO-relaxation measurements, *Biochemistry 38*, 10567−10577.
30. Hare, B. J., Wyss, D. F., Osburne, M. S., Kern, P. S., Reinharz, E. L., and Wagner, G. (1999) Structure, specificity and CDR mobility of a class II restricted single-chain T-cell receptor, *Nat. Struct. Biol. 6*, 574−581.
31. Ye, J., Mayer, K. L., and Stone, M. J. (1999) Backbone dynamics of the human CC-chemokine eotaxin, *J. Biomol. NMR 15*, 115−124.
32. Lee, A. L., Kinnear, S. A., and Wand, A. J. (2000) Redistribution and loss of side chain entropy upon formation of a calmodulin-peptide complex, *Nat. Struct. Biol. 7*, 72−77.
33. Gao, G., Semenchenko, V., Arumugam, S., and Van Doren, S. R. (2000) Tissue inhibitor of metalloproteinases-1 undergoes microsecond to millisecond motions at sites of matrix metalloproteinase-induced fit, *J. Mol. Biol. 301*, 537−552.
34. Lipari, G., and Szabo, A. (1982) Model-Free Approach to the Interpretation of Nuclear Magnetic Resonance Relaxation in Macromolecules. 1. Theory and Range of Validity, *J. Am. Chem. Soc. 104*, 4546−4559.
35. Clore, G. M., Szabo, A., Bax, A., Kay, L. E., Driscoll, P. C., and Gronenborn, A. M. (1990) Deviations from the simple two-parameter model-free approach to the interpretation of nitrogen-15 nuclear magnetic relaxation of proteins, *J. Am. Chem. Soc. 112*, 4989−4991.
36. Lipari, G., and Szabo, A. (1982) Model-Free Approach to the Interpretation of Nuclear Magnetic Resonance Relaxation in Macromolecules. 2. Analysis of Experimental Results, *J. Am. Chem. Soc. 104*, 4559−4570.
37. Bracken, C., Carr, P. A., Cavanagh, J., and Palmer, A. G., 3rd. (1999) Temperature Dependence of Intramolecular Dynamics of the Basic Leucine Zipper of GCN4: Implications for the Entropy of Association with DNA, *J. Mol. Biol. 285*, 2133−2146.
38. Ishima, R., and Nagayama, K. (1995) Protein Backbone Dynamics Revealed by Quasi Spectral Density Function Analysis of Amide N-15 Nuclei, *Biochemistry 34*, 3162−3171.

39. Farrow, N. A., Zhang, O., Szabo, A., Torchia, D. A., and Kay, L. E. (1995) Spectral density function mapping using ^{15}N relaxation data exclusively, *J. Biomol. NMR 6*, 153−162.
40. Peng, J. W., and Wagner, G. (1995) Frequency Spectrum of NH Bonds in Eglin C from Spectral Density Mapping at Multiple Fields, *Biochemistry 34*, 16733−16752.
41. Lefevre, J.-F., Dayie, K. T., Peng, J. W., and Wagner, G. (1996) Internal Mobility in the Partially Folded DNA Binding and Dimerization Domains of GAL4: NMR Analysis of the N-H Spectral Density Functions, *Biochemistry 35*, 2674−2686.
42. Tolman, J. R., Flanagan, J. M., Kennedy, M. A., and Prestegard, J. H. (1997) NMR evidence for slow collective motions in cyanometmyoglobin.[comment], *Nat. Struct. Biol. 4*, 292−297.
43. Tolman, J. R., Al-Hashimi, H. M., Kay, L. E., and Prestegard, J. H. (2001) Structural and dynamic analysis of residual dipolar coupling data for proteins, *J. Am. Chem. Soc. 123*, 1416−1424.
44. Wang, L., Pang, Y., Holder, T., Brender, J. R., Kurochkin, A. V., and Zuiderweg, E. R. (2001) Functional dynamics in the active site of the ribonuclease binase, *Proc. Natl. Acad. Sci. U.S.A. 98*, 7684−7689.
45. Stone, J. M., Trotochaud, A. E., Walker, J. C., and Clark, S. E. (1998) Control of meristem development by CLAVATA1 receptor kinase and kinase-associated protein phosphatase interaction, *Plant Physiol. 117*, 1217−1225.
46. Lee, G., Li, J., Walker, J. C., and Van Doren, S. R. (2003) ^{1}H, ^{13}C and ^{15}N resonance assignments of kinase-interacting FHA domain from Arabidopsis phosphatase KAPP, *J. Biomol. NMR. 25*, 253−254.
47. Farrow, N. A., Muhandiram, R., Singer, A. U., Pascal, S. M., Kay, C. M., Gish, G., Shoelson, S. E., Pawson, T., Forman-Kay, J. D., and Kay, L. E. (1994) Backbone Dynamics of a Free and a Phosphopeptide-Complexed Src Homology 2 Domain Studied by ^{15}N Relaxation, *Biochemistry 33*, 5984−6003.
48. Boyd, J., Hommel, U., and Campbell, I. D. (1990) Influence of cross-correlation between dipolar and anisotropic chemical shift relaxation mechanisms upon longitudinal relaxation rates of ^{15}N in macromolecules, *Chem. Phys. Lett. 175*, 477−482.
49. Sklenar, V., Piotto, M., Leppik, R., and Saudek, V. (1993) Gradient-Tailored Water Suppression for ^{1}H-^{15}N HSQC Experiments Optimized to Retain Full Sensitivity, *J. Magn. Reson. A 102*, 241−245.
50. Barbato, G., Ikura, M., Kay, L. E., Pastor, R. W., and Bax, A. (1992) Backbone dynamics of calmodulin studied by 15N relaxation using inverse detected two-dimensional NMR spectroscopy: the central helix is flexible, *Biochemistry 31*, 5269−5278.
51. Loria, J. P., Rance, M., and Palmer, A. G., 3rd. (1999) A Relaxation-Compensated Carr-Purcell-Meiboom-Gill Sequence for Characterizing Chemical Exchange by NMR Spectroscopy, *J. Am. Chem. Soc. 121*, 2331−2332.
52. Loria, J. P., Rance, M., and Palmer, A. G., 3rd. (1999) A TROSY CPMG sequence for characterizing chemical exchange in large proteins, *J. Biomol. NMR 15*, 151−155.
53. Delaglio, F., Grzesiek, S., Vuister, G. W., Zhu, G., Pfeifer, J., and Bax, A. (1995) NMRPipe: a multidimensional spectral processing system based on UNIX pipes, *J. Biomol. NMR 6*, 277−293.
54. Goddard, T. D., and Kneller, D. G. (2000) *SPARKY*, University of California, San Francisco.
55. Palmer, A. G., 3rd, Rance, M., and Wright, P. E. (1991) Intramolecular Motions of a Zinc Finger DNA-Binding Domain from Xfin Characterized by Proton-Detected Natural Abundance ^{13}C Heteronuclear NMR Spectroscopy, *J. Am. Chem. Soc. 113*, 4371−4380.
56. Dosset, P., Hus, J. C., Blackledge, M., and Marion, D. (2000) Efficient analysis of macromolecular rotational diffusion from heteronuclear relaxation data, *J. Biomol. NMR 16*, 23−28.
57. Pawley, N. H., Wang, C., Koide, S., and Nicholson, L. K. (2001) An improved method for distinguishing between anisotropic tumbling and chemical exchange in analysis of 15N relaxation parameters, *J. Biomol. NMR 20*, 149−165.
58. Tjandra, N., Szabo, A., and Bax, A. (1996) Protein Backbone Dynamics and ^{15}N Chemical Shift Anisotropy from Quantitative Measurement of Relaxation Interference Effects, *J. Am. Chem. Soc. 118*, 6986−6991.
59. Fushman, D., and Cowburn, D. (1998) Model-Independent Analysis of ^{15}N Chemical Shift Anisotropy from NMR Relaxation Data. Ubiquitin as a Test Example, *J. Am. Chem. Soc. 120*, 7109−7110.
60. Volkman, B. F., Alam, S. L., Satterlee, J. D., and Markley, J. L. (1998) Solution structure and backbone dynamics of component IV of Glycerea dibranchiata monomeric hemoglobin-CO, *Biochemistry 37*, 10906−10919.
61. d'Auvergne, E. J., and Gooley, P. R. (2003) The use of model selection in the model-free analysis of protein dynamics, *J. Biomol. NMR 25*, 25−39.
62. Akaike, H. (1973) in *Information theory and an extension of the maximum likelihood principle* (Petrov, B. N., Csaki, F., Eds.) pp 267−281, Academiai Kiado, Budapest.
63. Larsson, G., Martinez, G., Schleucher, J., and Wijmenga, S. S. (2003) Detection of nano-second internal motion and determination of overall tumbling times independent of the time scale of internal motion in proteins from NMR relaxation data, *J. Biomol. NMR 27*, 291−312.
64. Hansen, M. R., Hanson, P., and Pardi, A. (2000) Filamentous bacteriophage for aligning RNA, DNA, and proteins for measurement of nuclear magnetic resonance dipolar coupling interactions, *Methods Enzymol. 317*, 220−240.
65. Rückert, M., and Otting, G. (2000) Alignment of Biological Macromolecules in Novel Nonionic Liquid Crystalline Media for NMR Experiments, *J. Am. Chem. Soc. 122*, 7793−7797.
66. Oh, M. H., Ray, W. K., Huber, S. C., Asara, J. M., Gage, D. A., and Clouse, S. D. (2000) Recombinant brassinosteroid insensitive 1 receptor-like kinase autophosphorylates on serine and threonine residues and phosphorylates a conserved peptide motif in vitro, *Plant Physiol. 124*, 751−766.
67. Jin, D., Andrec, M., Montelione, G. T., and Levy, R. M. (1998) Propagation of experimental uncertainties using the Lipari-Szabo model-free analysis of protein dynamics, *J. Biomol. NMR 12*, 471−492.
68. Zweckstetter, M., and Bax, A. (2000) Prediction of Sterically Induced Alignment in a Dilute Liquid Crystalline Phase: Aid to Protein Structure Determination by NMR, *J. Am. Chem. Soc. 122*, 3791−3792.
69. Kay, L. E., Torchia, D. A., and Bax, A. (1989) Backbone Dynamics of Proteins as Studied by ^{15}N Inverse Detected Heteronuclear NMR Spectroscopy: Application to Staphylococcal Nuclease, *Biochemistry 28*, 8972−8979.
70. Blackledge, M., Cordier, F., Dosset, P., and Marion, D. (1998) Precision and Uncertainty in the Characterization of Anisotropic Rotational Diffusion by ^{15}N Relaxation, *J. Am. Chem. Soc. 120*, 4538−4539.
71. Dayie, K. T., Wagner, G., and Lefevre, J. F. (1996) Theory and practice of nuclear spin relaxation in proteins, *Annu. Rev. Phys. Chem. 47*, 243−282.
72. Fushman, D., Weisemann, R., Thüring, H., and Rüterjans, H. (1994) Backbone dynamics of ribonuclease T1 and its complex with 2′GMP studied by two-dimensional heteronuclear NMR spectroscopy, *J. Biomol. NMR 4*, 61−78.
73. Buchberger, A., Howard, M. J., Freund, S. M., Proctor, M., Butler, P. J., Fersht, A. R., and Bycroft, M. (2000) Biophysical characterization of elongin C from Saccharomyces cerevisiae, *Biochemistry 39*, 11137−11146.
74. Tugarinov, V., Liang, Z., Shapiro, Y. E., Freed, J. H., and Meirovitch, E. (2001) A structural mode-coupling approach to 15N NMR relaxation in proteins, *J. Am. Chem. Soc. 123*, 3055−3063.
75. Vugmeyster, L., Raleigh, D. P., Palmer, A. G., 3rd, and Vugmeister, B. E. (2003) Beyond the decoupling approximation in the model free approach for the interpretation of NMR relaxation of macromolecules in solution, *J. Am. Chem. Soc. 125*, 8400−8404.
76. Wang, P., Byeon, I. J., Liao, H., Beebe, K. D., Yongkiettrakul, S., Pei, D., and Tsai, M. D. (2000) II. Structure and specificity of the interaction between the FHA2 domain of Rad53 and phosphotyrosyl peptides, *J. Mol. Biol. 302*, 927−940.
77. Yongkiettrakul, S., Byeon, I. J., and Tsai, M. D. (2004) The ligand specificity of yeast Rad53 FHA domains at the +3 position is determined by nonconserved residues, *Biochemistry 43*, 3862−3869.
78. Olejniczak, E. T., Zhou, M. M., and Fesik, S. W. (1997) Changes in the NMR-derived motional parameters of the insulin receptor substrate 1 phosphotyrosine binding domain upon binding to an interleukin 4 receptor phosphopeptide, *Biochemistry 36*, 4118−4124.
79. Durocher, D., Henckel, J., Fersht, A. R., and Jackson, S. P. (1999) The FHA domain is a modular phosphopeptide recognition motif, *Mol. Cell 4*, 387−394.

80. Williams, D. C., Jr., Benjamin, D. C., Poljak, R. J., and Rule, G. S. (1996) Global Changes in Amide Hydrogen Exchange Rates for a Protein Antigen in Complex with Three Different Antibodies, *J. Mol. Biol. 257*, 866−876.
81. Trotochaud, A. E., Hao, T., Wu, G., Yang, Z., and Clark, S. E. (1999) The CLAVATA1 Receptor-like kinase requires CLAVATA3 for its assembly into a signaling Complex that includes KAPP and a Rho -related protein, *Plant Cell 11*, 393−405.
82. Jinn, T.-L., Stone, J. M., and Walker, J. C. (2000) HAESA, and Arabidopsis leucine-rich repeat receptor kinase, controls floral organ abscission, *Genes Dev. 14*, 108−117.
83. Arkin, M. R., Randal, M., DeLano, W. L., Hyde, J., Luong, T. N., Oslob, J. D., Raphael, D. R., Taylor, L., Wang, J., McDowell, R. S., Wells, J. A., and Braisted, A. C. (2003) Binding of small molecules to an adaptive protein-protein interface, *Proc. Natl. Acad. Sci. U.S.A. 100*, 1603−1608.
84. Shiu, S. H., and Bleecker, A. B. (2001) Receptor-like kinases from Arabidopsis form a monophyletic gene family related to animal receptor kinases, *Proc. Natl. Acad. Sci. U.S.A. 98*, 10763−10768.
85. Berjanskii, M. V., Riley, M. I., and Van Doren, S. R. (2002) Hsc70-interacting HPD loop of the J domain of polyomavirus T antigens fluctuates in psec to nsec and μsec to msec, *J. Mol. Biol. 321*, 503−516.

BI050414A